

A long-period transiting substellar companion in the super-Jupiters to brown dwarfs mass regime and a prototypical warm-Jupiter detected by TESS .[★]

Matías I. Jones¹, Yared Reinartz^{2,4,15}, Rafael Brahm^{3,4,5}, Marcelo Tala Pinto^{3,4}, Jan Eberhardt¹⁵, Felipe Rojas¹², Amaury H. M. J. Triaud¹⁴, Arvind F. Gupta^{7,8}, Carl Ziegler⁹, Melissa J. Hobson^{4,15}, Andrés Jordán^{3,4,5}, Thomas Henning¹⁵, Trifon Trifonov^{15,16}, Martin Schlecker¹⁷, Néstor Espinoza¹⁸, Pascal Torres-Miranda¹², Paula Sarkis¹⁵, Solène Ulmer-Moll^{23,24}, Monika Lendl²³, Murat Uzundag⁶, Maximiliano Moyano², Katharine Hesse¹⁹, Douglas A. Caldwell^{32,33}, Avi Shporer²⁰, Michael B. Lund³⁹, Jon M. Jenkins³², Sara Seager^{20,35,36}, Joshua N. Winn³⁷, George R. Ricker²⁰, Christopher J. Burke²⁰, Pedro Figueira²³, Angelica Psaridi²³, Khaled Al Moulla²³, Dany Mounzer²³, Matthew R. Standing²¹, David V. Martin²², Georgina Dransfield¹⁴, Thomas Baycroft¹⁴, Diana Dragomir²⁷, Gavin Boyle^{30,38}, Vincent Suc^{3,4,38}, Andrew W. Mann¹¹, Mathilde Timmermans²⁸, Elsa Ducrot²⁹, Matthew J. Hooton³⁰, Sebastián Zuñiga-Fernández²⁸, Daniel Sebastian¹⁴, Michael Gillon²⁸, Didier Queloz^{30,31}, Joe Carson¹³, and Jack J. Lissauer³²

(Affiliations can be found after the references)

ABSTRACT

We report on the confirmation and follow-up characterization of two long-period transiting substellar companions on low-eccentricity orbits around TIC 4672985 and TOI-2529, whose transit events were detected by the TESS space mission. Ground-based photometric and spectroscopic follow-up from different facilities, confirmed the substellar nature of TIC 4672985 *b*, a massive gas giant, in the transition between the super-Jupiters and brown-dwarfs mass regime. From the joint analysis we derived the following orbital parameters: $P = 69.0480^{+0.0004}_{-0.0005}$ d, $M_p = 12.74^{+1.01}_{-1.01}$ M_J , $R_p = 1.026^{+0.065}_{-0.067}$ R_J and $e = 0.018^{+0.004}_{-0.004}$. In addition, the RV time series revealed a significant trend at the ~ 350 m s⁻¹ yr⁻¹ level, which is indicative of the presence of a massive outer companion in the system. TIC 4672985 *b* is a unique example of a transiting substellar companion with a mass above the deuterium-burning limit, located beyond 0.1 AU and in a nearly circular orbit. These planetary properties are difficult to reproduce from canonical planet formation and evolution models. For TOI-2529 *b*, we obtained the following orbital parameters: $P = 64.5949^{+0.0003}_{-0.0003}$ d, $M_p = 2.340^{+0.197}_{-0.195}$ M_J , $R_p = 1.030^{+0.050}_{-0.050}$ R_J and $e = 0.021^{+0.024}_{-0.015}$, making this object a new example of a growing population of transiting warm giant planets.

Key words. Techniques: radial velocities – Techniques: photometric – Planets and satellites: gaseous planets – Planets and satellites: detection – Planets and satellites: composition

1. Introduction

Giant planets ($M_p \gtrsim 0.3 M_J$) with orbital period between ~ 10 – 200 d, also known as warm Jupiters (WJs), are excellent targets for measuring their bulk composition (e.g. Fortney et al. 2007), characterizing their atmospheric abundances, and studying their formation and evolution mechanisms (e.g., Knierim et al. 2022). In particular, they are less affected by the strong stellar irradiation and tidal interactions with the host star, than their innermost siblings, the so-called hot Jupiters. It is already well established that the strong insolation ($f_p \gtrsim 2 \times 10^8$ [erg s⁻¹ cm⁻²]; Demory & Seager 2011) received by hot Jupiters is associated with abnormally large radii, known as radius inflation (e.g. Baraffe et al. 2010; Laughlin et al. 2011), which in turn are due to delayed cooling and/or energy deposition in the planetary interior. The latter process might even lead to a planet reinflation after the host star evolves off the main sequence (Grunblatt et al. 2017; Komacek et al. 2020). However, although different mechanisms have been proposed to explain this observational feature, such as

tidal heating (e.g. Bodenheimer et al. 2001; Jackson et al. 2008) and ohmic dissipation (e.g. Batygin & Stevenson 2010; Thorngrén & Fortney 2018), they are not well understood (e.g. Sarkis et al. 2021). For these reasons, it is very challenging to determine the bulk composition of hot Jupiters based on their current radius and mass. Similarly, the strong tidal interactions with the host star, tend to circularize and synchronize their orbits (e.g., Rasio & Ford 1996; Guillot et al. 1996), thus hiding important clues about their formation and evolution pathways, such as their primordial orbital eccentricity and stellar obliquity (e.g., Albrecht et al. 2022). Thus, detecting WJs and characterizing their orbital properties can help us to distinguish different migration mechanisms, such as angular momentum exchange with the proto-planetary disk (e.g., Ward 1997) and high-eccentricity migration scenarios (e.g. Rasio & Ford 1996; Beaugé & Nesvorný 2012), both leading to short-period planets ($P \lesssim 10$ d) in nearly circular orbits. In this sense, although transiting WJs are rare (mainly because of their low transit probability) and more difficult to characterize than hot Jupiters (due to their longer orbital periods), they provide very valuable information for understanding giant planet formation and their orbital evolution (e.g., Petrovich & Tremaine 2016).

In this work we present the discovery, confirmation and characterization via ground-based photometric and spectroscopic

[★] Based on observations collected at La Silla - Paranal Observatory under programs IDs 105.20GX.001, 106.212H.001, 106.21ER.001 and 108.22A8.001 and through the Chilean Telescope Time under programs IDs CN2020B-21, CN2021A-14, CN2021B-23, CN2022A-33 and CN2022B-33

follow-up of two Jupiter-size transiting substellar objects, detected by the Transiting Exoplanet Survey Satellite (TESS ; Ricker et al. 2015) mission around TOI-2529 (TIC 269333648; TYC 8147-1020-1) and TIC 4672985 (TYC 5288-103-1). The paper is structured as follows. In sections 2 and 3 we present the TESS and ground-based photometric data. In sections 4 and 5 we describe the ground-based speckle imaging and spectroscopic follow-up, respectively. The derived stellar parameters are described in section 6, the results from the joint fit in section 7 and the discussion in section 8. Finally, the summary and conclusions are presented in section 9.

2. TESS photometry

We identified the transit signal of TIC 4672985 in the 30-minutes-cadence full-frame image (FFI) data generated by the Science Processing Operations Center at NASA Ames Research Center (Jenkins et al. 2016), obtained in sector 4 of the TESS primary mission. A query to the Gaia DR3 (Gaia Collaboration et al. 2022) archive revealed three stars within 42 arcsec (corresponding to two pixels), but all of them are fainter by ~ 7 magnitudes than TIC 4672985 (≥ 600 times fainter in the G band). No significant contamination from nearby stars is therefore expected. For this object, we adopted a simple aperture photometry of two pixels, meaning that only the pixels whose center fall within this radius are included (see Figure 1).

Similarly, we identified a total of three transit events in the TOI-2529 FFI TESS data obtained in sector 8 (30-minute cadence) of the primary mission, and in sectors 34 and 63 of the extended mission, with a cadence of 10 and 2 minutes, respectively. For this star, we used a rectangular aperture to prevent different stars from contaminating the aperture in different sectors (see Figure 1). However, we found two contaminating stars within the photometry aperture in all three sectors, with $G = 15.6$ ($\Delta\text{mag} = 4.4$) and $G = 16.2$ ($\Delta\text{mag} = 5.0$), leading to a combined fractional flux of $\sim 3\%$. These two signals were identified in an effort to characterize warm transiting planets as part of the Warm gl-aNts with tEss (WINE) collaboration (Brahm et al. 2019; Brahm et al. 2023). The light curves for these two stars in all four TESS sectors were generated with the *tesseract*¹ pipeline.

After extracting the light curve, we modeled the long-term continuum variability using a stochastic Gaussian process (GP). To do this, we first masked the transits and then fit the GP using a *celerite* Matern 3/2 kernel (Foreman-Mackey et al. 2017). We finally divided the extracted light curve by the resulting GP model to remove this long-term trend. The extracted photometry, GP model, and final detrended light curve for TIC 4672985 and TOI-2529 are presented in Figures 2 and 3.

3. Ground-based photometric data

We obtained ground-based photometric follow-up of TIC 4672985 to confirm the source of the transit detected in the TESS light curves, and also to refine the photometric ephemeris, which is particularly important for single-transit events. To do this, we used the available radial velocity data obtained in 2021 (see Sec. 5) in combination with the single TESS transit event in sector 4, to predict future transits that would be observable from the ground.

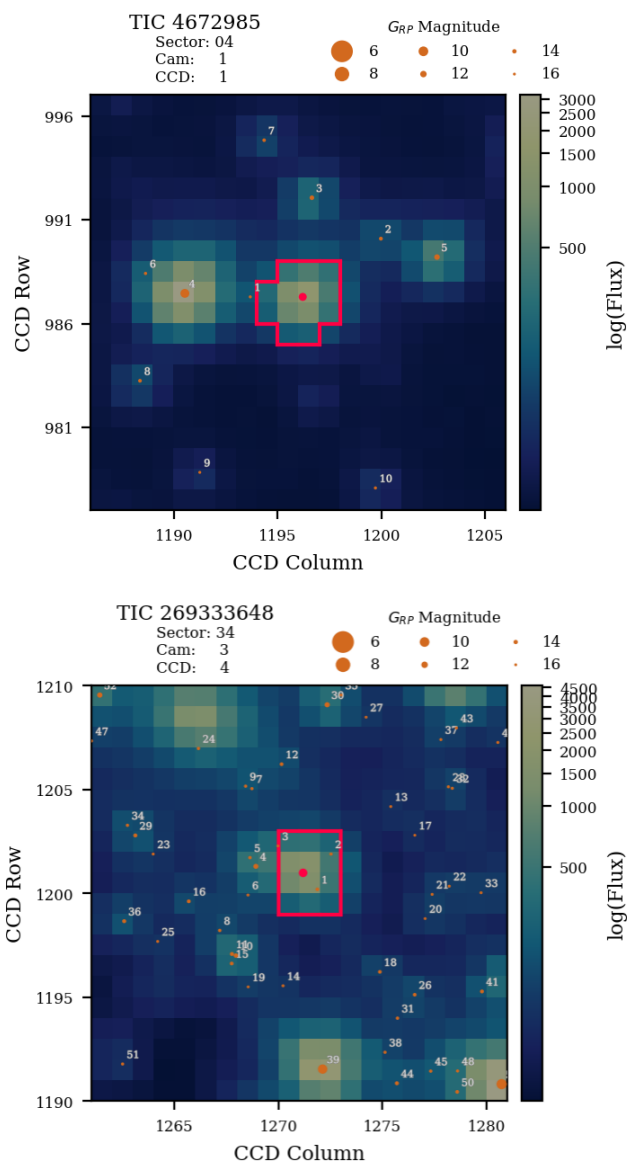


Fig. 1. TESS full-frame image of TIC 4672985, from sector 4 (upper panel) and of TOI-2529 in sector 34 (lower panel). Nearby sources detected by Gaia are also shown. The red box corresponds to the aperture used for the photometry extraction.

3.1. Callisto

Callisto is one of the six identical robotic one-meter telescopes of the Search for habitable Planets Eclipsing ULtra-coOL Stars (SPECULOOS; Delrez et al. 2018) network. Four of them, including Callisto, are installed at the Paranal observatory in Chile. The main scientific goal of SPECULOOS is the detection of transiting terrestrial planets in orbit around nearby (< 40 pc) late-type M and L-dwarfs. Each SPECULOOS telescope is equipped with a $2k \times 2k$ CCD, with a field of view of $12' \times 12'$ and a pixel scale of 0.35 arcsec/pix. We observed a transit egress of TIC 4672985 *b* with Callisto on 2021 September 8, using the *z* filter and with a cadence of 40 s. The extracted normalized photometry is presented in Figure 4.

¹ <https://github.com/astrofelipe/tesseract>

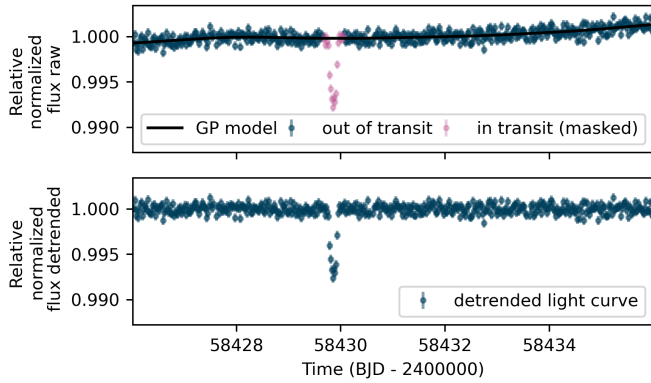


Fig. 2. Upper panel: TESS extracted light curve of TIC 4672985 observed in sector 4. The GP model used to correct for the long-term variability is overplotted (solid black line). Lower panel: Detrended TESS light curve.

3.2. OM-ES

The Observatoire Moana – El Sauce (OM-ES) facility is an equatorial robotic telescope with a 60 cm aperture, located at El Sauce Observatory, in Chile. OM-ES is equipped with a $2k \times 2k$ detector, with a pixel scale of of 0.7 arcsec/pix, and has a standard set of Sloan filters u', g', r', i' . Using this telescope, we observed a partial transit of TIC 4672985 in the night of 2021 November 16. For these observations, we used the i' filter, and we obtained an image every 49 s. The data reduction and photometry extraction was performed with a set of automated routines that were used previously in other facilities (e.g., [Brahm et al. 2020](#)). The extracted normalized photometric data are presented in Figure 4.

4. Speckle imaging

To search for potential sources of blending or flux contamination, we observed TIC 4672985 with the NN-Explore Exoplanet Stellar Speckle Imager (NESSI; [Scott et al. 2018](#)) on the WIYN 3.5 m telescope at Kitt Peak National Observatory, on 2019 October 12. We obtained one-minute sequences of short diffraction-limited exposures in each of the 832 nm and 562 nm filters with the red and blue NESSI cameras, respectively. The reconstructed speckle images were created following the procedures described in [Howell et al. \(2011\)](#). As we show in Figure 5, the computed 5σ contrast limits rule out companions brighter than $\Delta m_{562} = 3.9$ and $\Delta m_{832} = 4.4$ at separations greater than 0.5 arcsec and $\Delta m_{562} = 4.2$ and $\Delta m_{832} = 4.9$ outside of 1 arcsec.

Similarly, we searched for stellar companions to TOI-2529 with speckle imaging on the 4.1 m Southern Astrophysical Research (SOAR) telescope ([Tokovinin 2018](#)). To do this, we observed this star with the HRCam on 2021 October 1, in the Cousins I band. This observation was sensitive to a star that is fainter by 5.2 magnitudes at an angular distance of 1 arcsec from the target. More details of the observations within the SOAR TESS survey are available in [Ziegler et al. \(2020\)](#). The 5σ detection sensitivity and speckle autocorrelation functions from the observations are shown in Figure 6. No nearby stars were detected within 3 arcsec of TOI-2529 in the SOAR observations.

5. Ground-based spectroscopic follow-up

We performed a spectroscopic follow-up of these two stars, using four different high-resolution spectrographs. From the ob-

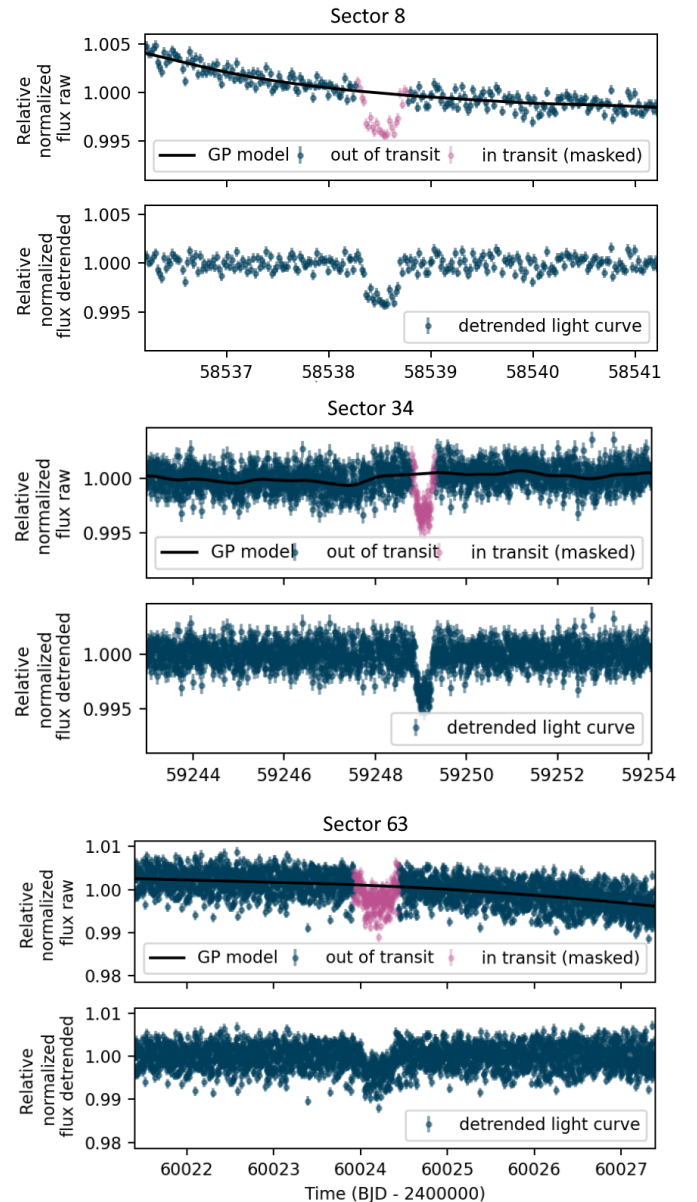


Fig. 3. Same as Fig. 2 but for TOI-2529 in sectors 8, 34 and 63 (upper, middle, and lower panel, respectively).

served spectra, we computed precision radial velocities (RVs), which were used to confirm the planetary nature of the observed photometric transits and to measure their masses. Similarly, from the cross-correlation function (CCF), we also measured the line bisectors (BVS; [Toner & Gray 1988](#)). The resulting RVs and BVS values, with their corresponding 1σ uncertainties are listed in Tables A.1 and A.2, and are also presented in Figures 7-10.

5.1. CHIRON

We observed TIC 4672985 and TOI-2529 with CHIRON ([Tokovinin et al. 2013](#)), as part of a large program in the context of the WINE collaboration. CHIRON is a high-resolution fiber-fed spectrograph mounted on the 1.5 m telescope at the Cerro Tololo Inter-american Observatory (CTIO) in Chile. We obtained a total of 24 spectroscopic epochs for TIC 4672985 and 21 epochs for TOI-2529. We adopted exposures times of 1800 s for the two stars, and we used the image-slicer mode,

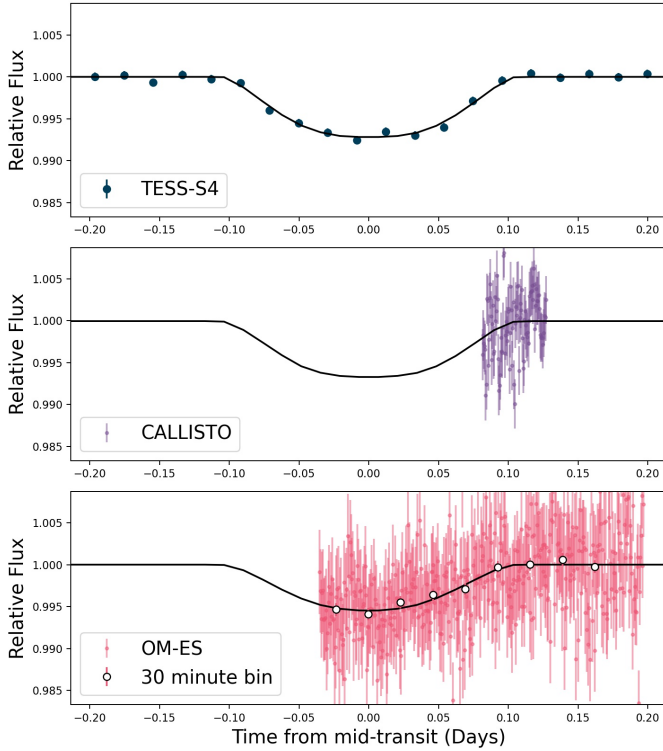


Fig. 4. Normalized photometric observations of TIC 4672985 during the transit. The data were obtained in TESS sector 4 (upper panel) and from ground-based telescopes (CALLISTO and OM-ES; middle and lower panels, respectively). The solid lines correspond to the transit models.

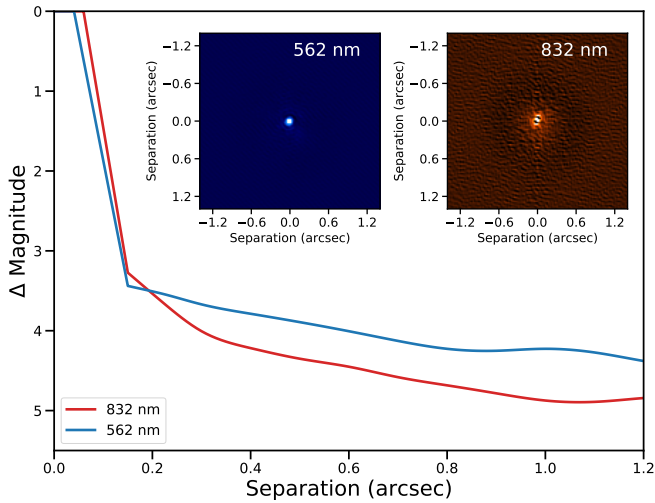


Fig. 5. Reconstructed NESSI speckle images for TIC 4672985. The observations were obtained simultaneously at 532 nm and 832 nm with the blue and red camera (upper left and right images). The corresponding 5σ contrast curves are overplotted (solid red and blue lines, respectively).

which delivers a spectral resolution of $R \sim 80,000$. The typical signal-to-noise-ratio (S/N) per extracted pixel was $\sim 10 - 20$ in the two cases, with corresponding mean RV uncertainties at the $\sim 13-15 \text{ m s}^{-1}$ level. The data were reduced using the CHIRON pipeline (Paredes et al. 2021) and the RVs were computed with the pipeline described in Jones et al. (2019).

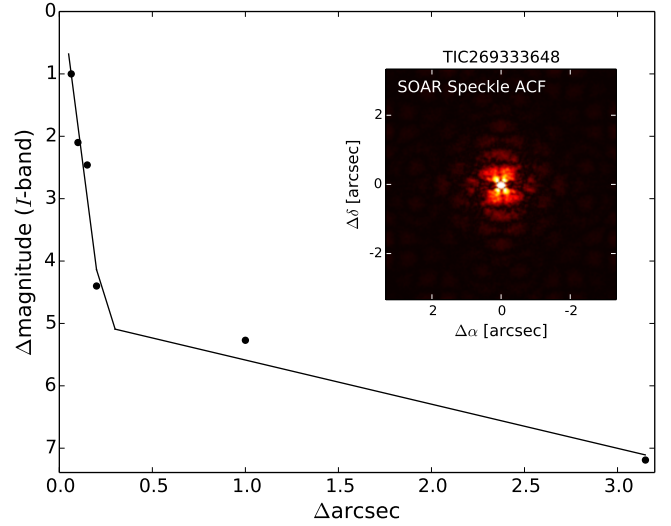


Fig. 6. Speckle autocorrelation function obtained in the I band at the SOAR telescope, for TOI-2529. The black dots correspond to the 5σ contrast curve. The solid line corresponds to the linear fit of the data at separations smaller and larger than ~ 0.2 arcsec.

5.2. FEROS

We collected a total of 20 individual spectra of TIC 4672985, between 2020 December 5 and 2022 January 8, with the Fiber-fed Extended Range Optical Spectrograph (FEROS; Kaufer et al. 1999) high-resolution spectrograph ($R \sim 48000$), installed at the 2.2 m telescope, at La Silla. The exposure times were between 900 s and 1800 s. FEROS is equipped with two fibers, allowing for either sky-background subtraction or simultaneous wavelength calibration. The latter is the observing mode we used in our observations. Similarly, we observed TOI-2529 a total of 17 times with FEROS between 2020 December 4 and 2021 December 30. For this star the exposure times were between 600 s and 900 s. The data were reduced with the CERES pipeline (Brahm et al. 2017a), which also automatically computes the stellar RV and BVS values. The typical uncertainty in the derived FEROS RVs is $\sim 7-8 \text{ m s}^{-1}$ for the two stars.

5.3. HARPS

The High Accuracy Radial velocity Planet Searcher (HARPS; Mayor et al. 2003) is a fibre-fed by the Cassegrain focus of the 3.6 m telescope at La Silla Observatory. Using this instrument, we obtained 27 spectra for TOI-2529 and 18 for TIC 4672985. We selected the high-resolution mode (1 arcsec fibre, leads to $R \sim 115,000$) and the simultaneous wavelength calibration for our observations. The exposure time was 900 s for TIC 4672985 and between 600 s and 900 s for TOI-2529. As for FEROS, the data reduction and RV computation was made with CERES. The mean RV uncertainty is $\sim 6 \text{ m s}^{-1}$ and 8 m s^{-1} , for TIC 4672985 and TOI-2529, respectively.

5.4. CORALIE

We collected a total of 29 spectra of TIC 4672985 using CORALIE (Queloz et al. 2000), which is mounted on the 1.2 m Leonhard Euler Telescope at La Silla observatory. CORALIE is an echelle high-resolution spectrograph that delivers a resolving power of $R \sim 60,000$. This instrument is also equipped with

two optical fibres, the second of which is fed by either a sky or a simultaneous calibration source, in this case, a Fabry-Perot interferometer. As for FEROS and HARPS, we used the latter configuration to correct for the night drift. The data reduction and RV computation was performed with the CORALIE data reduction software.

6. Stellar parameters

We derived the stellar properties of the two host stars, using the zonal atmospheric stellar parameters estimator (ZASPE; [Brahm et al. 2017b](#)) code, following an iterative procedure described in detail elsewhere (e.g., [Brahm et al. 2019](#); [Hobson et al. 2021](#)). Briefly, we first coadded the FEROS spectra to create a high S/N observed template of each star. We then used ZASPE to compare the resulting template with a grid of synthetic spectra from the ATLAS9 models ([Castelli & Kurucz 2003](#)). After exploring a wide parameter range, we derived a first set of stellar atmospheric parameters (T_{eff} , $\log g$, $[\text{Fe}/\text{H}]$ and $v \sin i$). Then, the physical stellar parameters (M_* , R_* , L_* , ρ_*) and the stellar age and visual extinction in the line of sight (A_V) were obtained by comparing the stellar broadband photometry, which was converted into absolute magnitude using the GAIA DR2 ([Gaia Collaboration et al. 2018](#)) parallaxes, with the synthetic magnitudes from the PARSEC stellar evolutionary models ([Bressan et al. 2012](#)). In this process we fixed the metallicity found in the first step and used the initial T_{eff} as a prior for this second step. We repeated this procedure in an iterative way until convergence was reached. The resulting atmospheric and physical parameters for the two stars are listed in Table 1. We note that for the rest of the paper, we adopt the ZASPE stellar parameters. For comparison, we also computed atmospheric and physical parameters for the two stars using the SPECIES code ([Soto et al. 2021](#)). They are also listed in Table 1. In general, the two methods agree very well. We note that the uncertainties listed in Table 1 correspond to the internal uncertainties obtained by the different methods we used, and they do not consider systematic errors. However, following [Tayar et al. \(2022\)](#), we add systematic uncertainties of 2% in quadrature to the stellar luminosity, an uncertainty of 4% to the stellar radius, an uncertainty of 5% to the stellar mass, and an uncertainty of 20% to the stellar age in the following sections. This significantly affects the final planet parameters and their corresponding uncertainties.

Finally, we performed a periodogram analysis of the V-band all sky automated survey (ASAS; [Pojmanski 1997](#)) and the all-sky automated survey for supernovae (ASAS-SN; [Kochanek et al. 2017](#)) photometric data of these two stars to estimate the stellar age via gyrochronology. No significant periodicity was found in the periodogram of either star (see Fig. A.4 and A.3), and their rotational period could therefore not be derived.

7. Joint photometric and radial velocity analysis

We jointly modeled the ground- and space-based photometry with the derived RVs for the two systems presented here. To do this we used *juliet* ([Espinoza et al. 2019](#)), a python-based package that employs Bayesian inference and nested sampling to achieve model fitting and comparison. *juliet* uses the *radvel* package ([Fulton et al. 2018](#)) for the RV data modeling, and *batman* ([Kreidberg 2015](#)) for the photometric transit model. In addition, we used the *dynesty* package ([Speagle 2020](#)), which is incorporated in *juliet*, to sample the posterior distributions. We used uniform priors for the orbital and transit

Table 1. Stellar parameters.

Parameter	TOI-2529	TIC 4672985	Source
T_{eff} [K]	5802^{+60}_{-52}	5757^{+72}_{-65}	ZASPE
	5793^{+50}_{-50}	5754^{+66}_{-66}	SPECIES
$\log g$ [dex]	$4.03^{+0.01}_{-0.01}$	$4.32^{+0.02}_{-0.02}$	ZASPE
	$4.05^{+0.08}_{-0.08}$	$4.32^{+0.08}_{-0.08}$	SPECIES
$[\text{Fe}/\text{H}]$ [dex]	$0.10^{+0.03}_{-0.03}$	$0.14^{+0.05}_{-0.05}$	ZASPE
	$0.13^{+0.05}_{-0.05}$	$0.20^{+0.04}_{-0.04}$	SPECIES
M_* [M_{\odot}]	$1.11^{+0.01}_{-0.02}$	$1.01^{+0.03}_{-0.03}$	ZASPE
	$1.13^{+0.02}_{-0.02}$	$1.04^{+0.02}_{-0.02}$	SPECIES
R_* [R_{\odot}]	$1.70^{+0.02}_{-0.03}$	$1.15^{+0.01}_{-0.01}$	ZASPE
	$1.69^{+0.03}_{-0.03}$	$1.15^{+0.02}_{-0.02}$	SPECIES
L_* [L_{\odot}]	$2.91^{+0.15}_{-0.12}$	$1.30^{+0.06}_{-0.05}$	ZASPE
	$2.88^{+0.12}_{-0.11}$	$1.26^{+0.04}_{-0.04}$	SPECIES
Age [Gyr]	$7.23^{+0.41}_{-0.55}$	$7.71^{+1.45}_{-1.46}$	ZASPE
	$7.05^{+0.40}_{-0.34}$	$6.82^{+1.02}_{-0.98}$	SPECIES
A_V [mag]	$0.45^{+0.08}_{-0.06}$	$0.11^{+0.07}_{-0.06}$	ZASPE
	$0.42^{+0.10}_{-0.10}$	$0.07^{+0.10}_{-0.10}$	SPECIES
$v \sin i$ [km s^{-1}]	$3.7^{+0.3}_{-0.3}$	$3.5^{+0.4}_{-0.4}$	ZASPE
T [mag]	10.669 ± 0.006	10.992 ± 0.007	TICv8 ^a
B [mag]	12.12 ± 0.16	...	Tycho-2 ^b
	...	12.275 ± 0.023	APASS ^c
V [mag]	11.53 ± 0.13	...	Tycho-2
	...	11.584 ± 0.014	APASS
G [mag]	11.190 ± 0.003	11.4391 ± 0.003	GAIA ^d
J [mag]	9.935 ± 0.024	10.354 ± 0.023	2MASS ^e
H [mag]	9.620 ± 0.026	10.059 ± 0.022	2MASS
K [mag]	9.489 ± 0.024	9.97 ± 0.023	2MASS

References. (a) : [Stassun et al. 2019](#); (b) : [Høg et al. 2000](#); (c) : [Munari et al. 2014](#); (d) : [Gaia Collaboration 2020](#); (e) : [Cutri et al. 2003](#)

parameters. Based on the effective temperature of both host stars and following ([Espinoza & Jordán 2016](#)), we adopted a logarithmic limb-darkening law for both ground- and space-based photometry, also setting uniform priors on the q_1 and q_2 parameters (see [Kipping 2013](#)). In the case of TIC 4672985, we fixed the dilution factor to 1, while in the case of TOI-2529, we fit this parameter by adopting a uniform prior based on the expected level of contamination by nearby sources (see Sec. 2). Following the approach presented in [Espinoza et al. \(2019\)](#), we used the estimated stellar density to constrain a/R_* , this time using a normal distribution prior, with μ and σ derived using ZASPE. Finally, we adopted uniform priors for the RV zeropoint and extra jitter, while for the photometric extra jitter, we used log-uniform priors. We note that for TIC 4672985, we also modeled the RV trend with a linear and quadratic trend. The resulting Bayesian evidence favored the quadratic model ($\Delta \log z = 6.1$). The prior and resulting posterior distributions of the pertinent parameters for TIC 4672985 b and TOI-2529 b are presented in Tables 2 and

3, respectively². Similarly, the transit models for TIC 4672985 *b* and TOI-2529 *b* are presented in Figures 4 and 11, respectively. Finally, for these two systems, no significant periodic signal is detected in the RV residuals (see Figures A.1 and A.2).

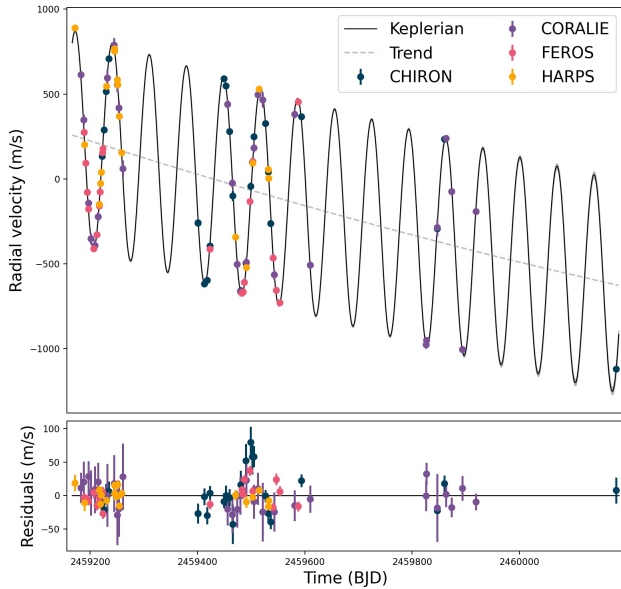


Fig. 7. RV curve of TIC4672985. The best Keplerian fit and the observed RV trend are overplotted.

8. Discussion

8.1. TOI-2529 *b* and TIC 4672985 *b* in the context of transiting giant planets

Figure 12 shows the mass-radius distribution of known³ transiting giant planets, with a mass and radius determination better than 20%, including the position of TOI-2529 *b* and TIC 4672985 *b*. For comparison, a solar metallicity, 1 Gyr old ATMO2020 isochrone (Phillips et al. 2020) is overplotted. The deuterium-burning limit ($\sim 11\text{--}16 M_J$; Spiegel et al. 2011) is also shown. TOI-2529 *b* is a new example of a growing population of well-characterized transiting giant planets with orbital periods $> 10 d$. Because this type of planets has a mild insolation level, they cool down slowly while losing their internal energy in the form of radiation. As a result, and after ~ 1 Gyr from their birth, they shrink to $\sim 1 R_J$ and reach an effective temperature between $\sim 200\text{--}500$ K. In contrast, closer-in gas giants remain significantly hotter and therefore have larger radii at a given age. These two different populations can be clearly distinguished in Figure 12, where hot Jupiters show a radius distribution between $\sim 1\text{--}2 R_J$, while most warm giant planets pile up around $\sim 1 R_J$. On the other hand, TIC 4672985 *b* is a unique example of a transiting warm planet that is in the transition between the super-Jupiter and the BD regime. Fig. 12 shows that this object stands

² For the equilibrium temperature we adopted a zero Bond albedo and $\beta = 1$; see Kaltenegger & Sasselov (2011)

³ Data from NASA Exoplanet Archive, as of June 30, 2023. We complemented this list with known transiting brown-dwarf (BDs) from Carmichael et al. (2021).

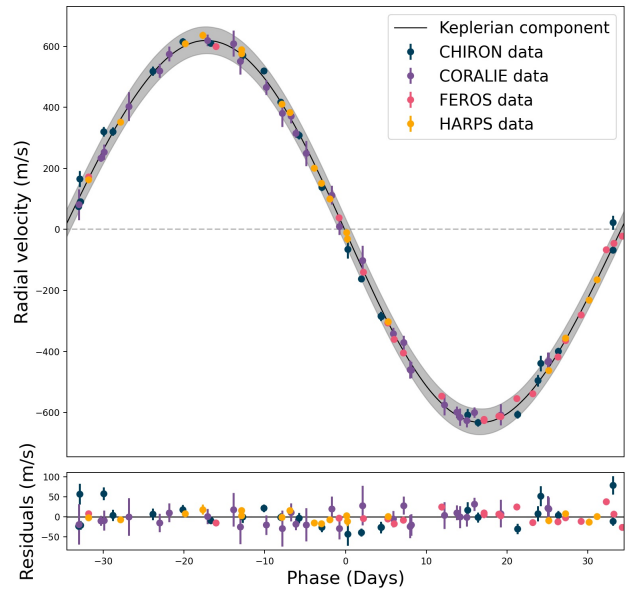


Fig. 8. Phase-folded RV curve for TIC 4672985, after subtracting the quadratic trend. The gray region corresponds to 1σ uncertainty in the best-fit model.

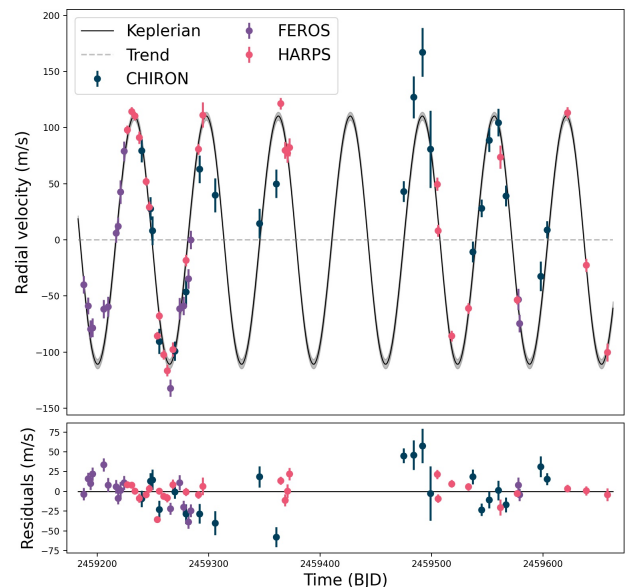


Fig. 9. Same as Fig. 7, but for TOI-2529.

alone in the deuterium-burning limit region among the population of warm transiting giant planets.

Similarly, Figure 13 shows the bulk density as a function of the planet mass. Again, there is a clear distinction between the hot and warm giant planets. Hot giants present a large scatter, with many examples of extremely low-density objects, as opposed to the warmer counterpart, which mainly follows a linear correla-

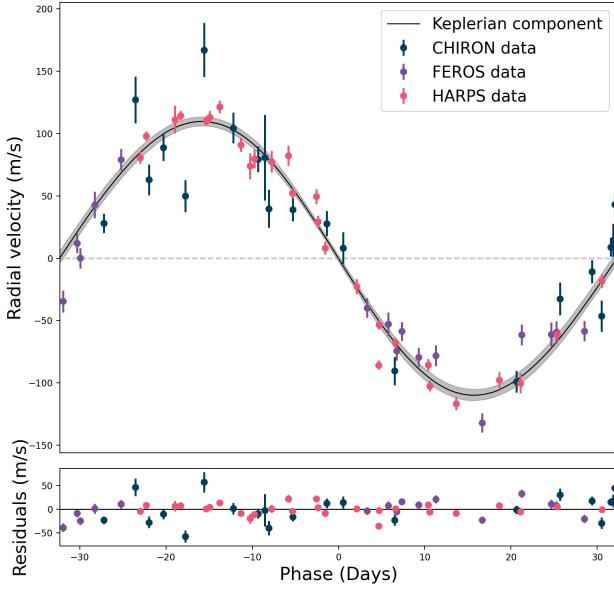


Fig. 10. Same as Fig. 8, but for TOI-2529.

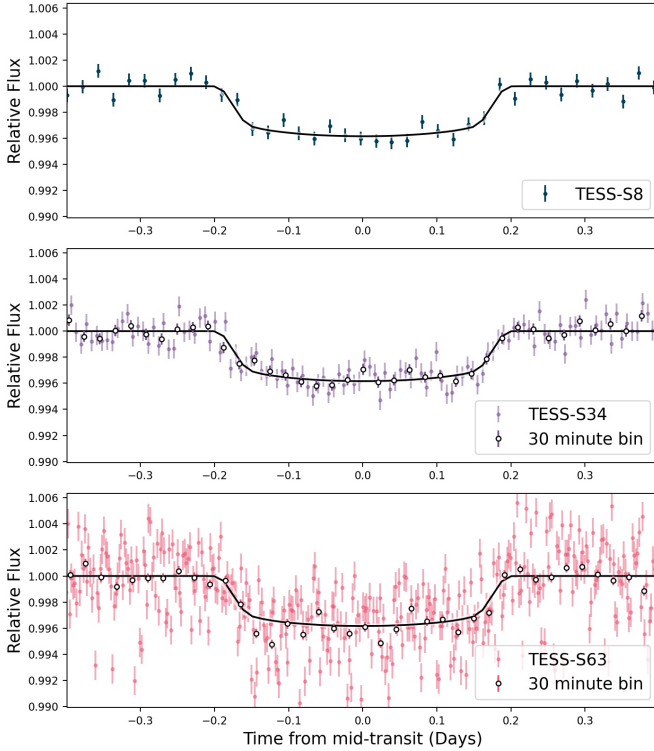


Fig. 11. Normalized TESS photometry of TOI-2529 around the transit in sectors 8, 34, and 63 (upper, middle, and lower panels, respectively). The 30-minute binned data and the best-fit transit model are overlaid.

tion between these two quantities in log-log space, as predicted by evolutionary models.

Finally, Figure 14 shows the eccentricity distribution as a function of the orbital separation. We included only planets

Table 2. TIC 4672985 Model Parameters

Parameter	Prior	Value
P (days)	$\mathcal{U}(68.9, 69.1)$	$69.0480^{+0.0004}_{-0.0005}$
T_0 (BJD - 2450000)	$\mathcal{U}(8429.7, 8429.8)$	$8429.8577^{+0.0016}_{-0.0016}$
e	$\mathcal{U}(0.0, 0.4)$	$0.018^{+0.004}_{-0.004}$
ω	$\mathcal{U}(0.0, 360.0)$	$126.3^{+11.3}_{-7.6}$
R_p/R_*	$\mathcal{U}(0.01, 0.15)$	$0.089^{+0.005}_{-0.004}$
b	$\mathcal{U}(0.0, 1.0)$	$0.90^{+0.01}_{-0.01}$
ρ_* (kg m^{-3})	$\mathcal{N}(1023.0, 57.999)$	$939.0^{+99.8}_{-101.8}$
K (m s^{-1})	$\mathcal{U}(500.0, 700.0)$	$625.4^{+3.3}_{-3.4}$
μ^{coralie} (m s^{-1})	$\mathcal{U}(-500.0, 500.0)$	$60.7^{+6.6}_{-6.2}$
σ^{coralie} (m s^{-1})	$\mathcal{U}(5.0, 40.0)$	$9.1^{+5.4}_{-2.8}$
μ^{chiron} (m s^{-1})	$\mathcal{U}(-500.0, 500.0)$	$28.7^{+6.1}_{-6.0}$
σ^{chiron} (m s^{-1})	$\mathcal{U}(0.0, 50.0)$	$24.1^{+5.9}_{-4.8}$
μ^{harps} (m s^{-1})	$\mathcal{U}(-500.0, 500.0)$	$-250.4^{+3.5}_{-3.2}$
σ^{harps} (m s^{-1})	$\mathcal{U}(0.0, 15.0)$	$9.5^{+2.8}_{-2.6}$
μ^{feros} (m s^{-1})	$\mathcal{U}(-500.0, 500.0)$	$215.2^{+4.1}_{-4.3}$
σ^{feros} (m s^{-1})	$\mathcal{U}(0.0, 25.0)$	$15.4^{+3.4}_{-3.1}$
$q^{\text{tess-S4}}$	$\mathcal{U}(0.0, 1.0)$	$0.53^{+0.32}_{-0.33}$
$q^{\text{DM-ES}}$	$\mathcal{U}(0.0, 1.0)$	$0.61^{+0.27}_{-0.28}$
q^{callisto}	$\mathcal{U}(0.0, 1.0)$	$0.47^{+0.36}_{-0.31}$
$q^{\text{tess-S4}}$	$\mathcal{U}(0.0, 1.0)$	$0.74^{+0.17}_{-0.23}$
$q^{\text{DM-ES}}$	$\mathcal{U}(0.0, 1.0)$	$0.12^{+0.14}_{-0.09}$
q^{callisto}	$\mathcal{U}(0.0, 1.0)$	$0.51^{+0.30}_{-0.31}$
$\sigma^{\text{tess-S4}}$ (ppm)	$\mathcal{J}(0.01, 1000.0)$	$1.0^{+18.8}_{-0.91}$
$\sigma^{\text{DM-ES}}$ (ppm)	$\mathcal{J}(0.01, 10000.0)$	$3.8^{+135.2}_{-3.7}$
σ^{callisto} (ppm)	$\mathcal{J}(0.01, 10000.0)$	$1818.2^{+562.0}_{-1385.4}$
rv_{slope} ($\text{m s}^{-1} \text{ d}^{-1}$)	$\mathcal{U}(-10.0, 10.0)$	$-0.94^{+0.01}_{-0.01}$
rv_{quad} ($\text{m s}^{-1} \text{ d}^{-2}$)	$\mathcal{U}(-0.1, 0.1)$	$0.00015^{+0.00004}_{-0.00004}$
a (AU)		$0.330^{+0.019}_{-0.019}$
R_p (R_J)		$1.026^{+0.067}_{-0.065}$
M_p (M_J)		$12.74^{+1.01}_{-1.01}$
T_{eq} (K)		$517.2^{+11.3}_{-11.2}$

Note: The instrumental zeropoints were computed after subtracting the RV mean value.

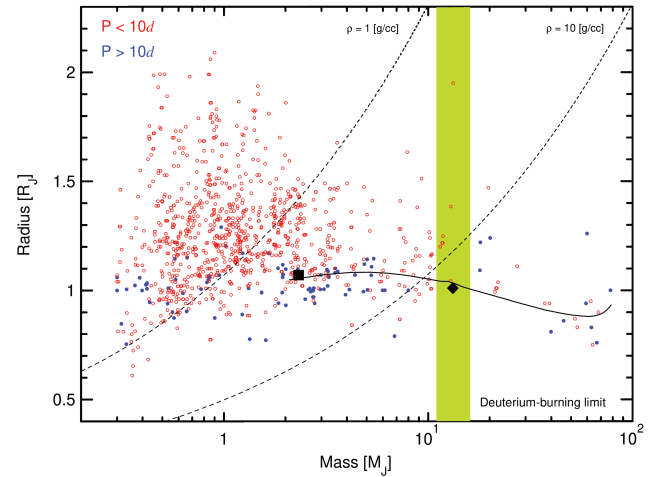
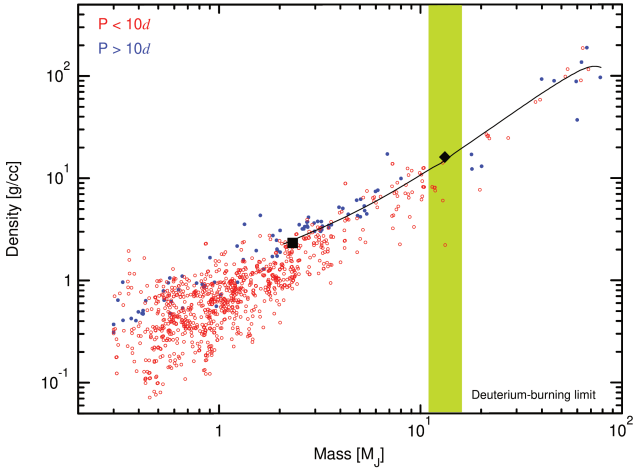


Fig. 12. Mass-radius distribution of known transiting giant planets as of June 30, 2023. The open red circles and blue dots correspond to orbital periods shorter and longer than 10 d, respectively. The positions of TIC 4672985 b (black diamond) and TOI-2529 b (black square) are also shown. The shaded area represents the theoretical deuterium-burning limit. The solid line corresponds to a 1 Gyr old and solar metallicity ATMO2020 isochrone. Two isodensity curves for 1 and 10 [gr cm^{-3}] are also plotted (dashed left and right lines, respectively).

Table 3. TOI-2529 model parameters

Parameter	Prior	Value
P (days)	$\mathcal{U}(64.5, 64.6)$	$64.5949^{+0.0003}_{-0.0003}$
T_0 (BJD - 2450000)	$\mathcal{U}(8538.5, 8538.6)$	$8538.5151^{+0.0046}_{-0.0041}$
e	$\mathcal{U}(0.0, 0.5)$	$0.021^{+0.024}_{-0.015}$
ω	$\mathcal{U}(0.0, 360.0)$	$103.8^{+100.5}_{-39.3}$
R_p/R_*	$\mathcal{U}(0.01, 0.15)$	$0.061^{+0.001}_{-0.001}$
b	$\mathcal{U}(0.0, 1.0)$	$0.68^{+0.03}_{-0.04}$
ρ_* (kg m^{-3})	$\mathcal{N}(328.7, 41.3)$	$326.0^{+40.7}_{-41.9}$
K (m s^{-1})	$\mathcal{U}(50.0, 200.0)$	$110.5^{+3.1}_{-3.2}$
μ^{harps} (m s^{-1})	$\mathcal{U}(-100.0, 100.0)$	$-17.8^{+2.6}_{-2.6}$
σ_w^{harps} (m s^{-1})	$\mathcal{U}(0.0, 15.0)$	$11.2^{+1.9}_{-1.6}$
μ^{feros} (m s^{-1})	$\mathcal{U}(-100.0, 100.0)$	$38.3^{+4.7}_{-5.2}$
σ_w^{feros} (m s^{-1})	$\mathcal{U}(0.0, 25.0)$	$17.3^{+2.6}_{-2.6}$
μ^{chiron} (m s^{-1})	$\mathcal{U}(-100.0, 100.0)$	$-32.9^{+6.3}_{-6.2}$
σ_w^{chiron} (m s^{-1})	$\mathcal{U}(10.0, 40.0)$	$27.2^{+5.5}_{-5.2}$
$\sigma_w^{\text{tess}} - S8$ (ppm)	$\mathcal{J}(0.01, 10000.)$	$444.8^{+49.9}_{-42.5}$
$\sigma_w^{\text{tess}} - S34$ (ppm)	$\mathcal{J}(0.01, 10000.)$	$673.2^{+25.0}_{-27.0}$
$\sigma_w^{\text{tess}} - S63$ (ppm)	$\mathcal{J}(0.01, 10000.)$	$2362.2^{+42.2}_{-38.6}$
q_1^{tess}	$\mathcal{U}(0.0, 1.0)$	$0.38^{+0.38}_{-0.28}$
q_2^{tess}	$\mathcal{U}(0.0, 1.0)$	$0.52^{+0.27}_{-0.29}$
$m_{\text{dilution}}^{\text{tess}}$	$\mathcal{U}(0.96, 0.98)$	$0.97^{+0.01}_{-0.01}$
a (AU)		$0.327^{+0.020}_{-0.020}$
R_p (R_J)		$1.030^{+0.050}_{-0.050}$
M_p (M_J)		$2.340^{+0.197}_{-0.195}$
T_{eq} (K)		$636.0^{+15.6}_{-15.7}$

Note: The instrumental zeropoints were computed after subtracting the RV mean value.


Fig. 13. Same as Fig. 12, but for the planet density.

with a mass determination⁴ better than 20% and an eccentricity uncertainty of $\sigma_e < 0.15$. While TOI 2529 *b* presents a low-eccentricity level, which is common among the population of low-mass giant planets orbiting beyond ~ 0.1 AU, TIC 4672985 *b* stands out as a unique massive warm substellar companion in a nearly circular orbit.

⁴ We included only transiting planets so as to have actual mass measurements rather than RV values of $M_p \sin i$ that only provide lower limits to M_p

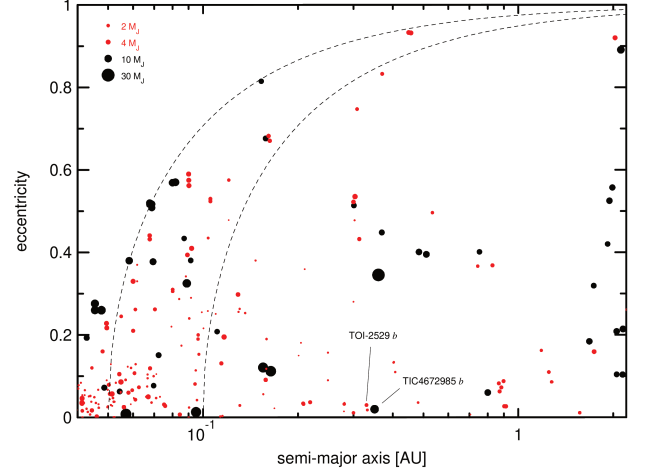


Fig. 14. Eccentricity distribution as a function of the orbital distance for known giant planets with eccentricity precision of $\sigma_e < 0.15$ and mass precision better than 20%, including TIC 4672985 *b* and TOI-2529 *b*. The size of the symbols is proportional to the square of the planet's mass. For more clarity, we split the data into two populations, with masses below and above 5 M_J (red and black dots, respectively). The dotted lines correspond to high-eccentricity migration pathways at constant angular momentum (e.g. Dong et al. 2021), with final orbital distance of 0.05 and 0.10 AU (left and right curves, respectively).

8.2. Internal composition of the planets

To study the composition of the planets presented here, we compared their radii with planet evolutionary models. In particular, we used the modules for experiments in stellar astrophysics (MESA; Paxton et al. 2011), and we generated different giant planet models, with a different envelope composition and core mass, and we also included the effect of the stellar irradiation. To do this, we used the updated⁵ version of the ρ - T OPAL tables (Rogers & Nayfonov 2002), with the extension to lower temperatures and densities from the SCvH equation of state (EOS) presented in Saumon et al. (1995). We note that we mimicked the presence of metals in the H/He SCvH EOS by setting an equivalent He content given by $Y' = Y + Z$, as shown in Chabrier & Baraffe (1997). Similarly, we employed the low-temperature opacity tables from Ferguson et al. (2005) and Freedman et al. (2008), coupled with the heavy element distribution of Grevesse & Sauval (1998). These tables also include the radiative opacities from molecules and grains. Finally, we adopted the solar metallicity $Z = 0.0152$ with the corresponding helium-scaled mass fraction: $Y = 0.2485 + 1.78 Z$, derived in Bressan et al. (2012), which is the one used by ZASPE (see Section 6).

We first created an adiabatically contracting model using the `create_initial_model` routine (Paxton et al. 2013), which builds a planetary model with a given initial radius and gas mass. In our calculations, we set the initial radius to 5 R_J for all the different models, with the possibility of including an inert rocky core with constant density. Finally, we evolved the different models for 8 Gyr, and also included the planet insolation. To do this, we implemented the `gray_irradiated` option inside the `atm` module, which uses the angle-averaged temperature profile described in Guillot (2010). This option includes both the stellar irradiation and the cooling flux from the planetary interior. Instead of using the current insolation value, we computed the incident flux received by the planet, by fixing the orbital dis-

⁵ https://opalopacity.llnl.gov/EOS_2005

tance to its current value, and we updated the host star luminosity in steps of 1 Gyr, using PARSEC stellar evolutionary models that matched the stellar parameters for each star, as derived here (see Table 1). This is particularly important for TOI-2529, which is in the subgiant phase, and therefore, its luminosity has increased significantly since the zero-age main sequence.

To study the composition of TOI-2529 *b*, we computed different models with a total mass of $2.34 M_J$. In our calculations, we included a coreless and a rocky core model with a different amount of metals in the H/He gas envelope (Z_{env}). Finally, we assumed that the age of the planet is the same as that of the host star, considering the very short lifetime of protoplanetary disks (e.g., Mamajek 2009). Figure 15 shows the position of TOI-2529 *b* in the age-radius diagram. Two different models with a $40 M_{\oplus}$ core with constant density of $20 \text{ [gr cm}^{-3}]$ and with different envelope compositions are overplotted. For comparison, a model with incident flux (f_{inc}) equal to zero is also shown. A possible model that reproduces the current radius of the planet well is the model with a rocky core, $Z_{\text{env}} = 0.019$ (the same as the host star) and with stellar irradiation. However, we note that different combinations of the core composition and Z_{env} can reproduce observed properties of the planet within the observational uncertainties in age and radius. By fixing the Z_{env} to 0.019 and the density of the core to $20 \text{ [gr cm}^{-3}]$, we found that core masses up to $\sim 100 M_{\oplus}$ match the observed age-radius of the planet within 1σ . This corresponds to a heavy element enrichment of $Z_p/Z_{\star} \sim 1\text{--}8$. We also note that even though TOI-2529 *b* is a WJ, the effect of the stellar irradiation plays an important role in its cooling evolution, and thus in its radius as a function of time. After ~ 1 Gyr, the effect of the delayed cooling due to the incident flux clearly leads to a radius that is $\sim 4\%$ larger than in the model without incident flux (blue line in Figure 15). Moreover, heat deposition from the stellar flux in the planet interior (e.g. Ginzburg & Sari 2016), would further slow the planet cooling rate down, and thus models with larger heavy element fraction would fit the observed radius of the planet better. Finally, and for comparison, a simple model of Jupiter (age = 4.6 Gyr) is overplotted (green line).

Similarly, Figure 16 shows the position of TIC 4672985 *b* in the age-radius diagram. Again, different models with different compositions, and including the stellar irradiation are shown. For comparison, we also included a model with $f_{\text{inc}} = 0$. We note that for this object we did not include a rocky core and we neglected the additional heating from deuterium burning, which can increase the luminosity and halt its contraction at early epochs ($\leq 50\text{--}100$ Myr; e.g. Chabrier et al. 2000; Paxton et al. 2011; Mollière & Mordasini 2012), but it has a negligible effect in the long-term evolution of the planet. Although a model with the same composition as of the host star matches the current position of TIC 4672985 *b* at the 1σ level, models with subsolar metallicity are clearly preferred. This means that no heavy-elements enrichment with respect to the parent star need be invoked.

9. Summary and conclusions

We used space- and ground-based photometry from different facilities, combined with precision RVs obtained from spectroscopic data collected with different instruments, to characterize two transiting giant planets orbiting the subgiant star TOI-2529 and the main-sequence star TIC 4672985. From the joint analysis we derived the following parameters for TOI-2529 *b*: $P = 64.5949^{+0.0003}_{-0.0003}$ d, $M_p = 2.340^{+0.197}_{-0.195} M_J$, $R_p = 1.030^{+0.050}_{-0.050} R_J$, and $e = 0.021^{+0.024}_{-0.015}$. With an equilibrium temperature of ~ 636 K due to a relatively low current insolation of $3.7 \times 10^7 \text{ [erg s}^{-1} \text{ cm}^{-2}]$, this planet is an excellent example of an emerging population of

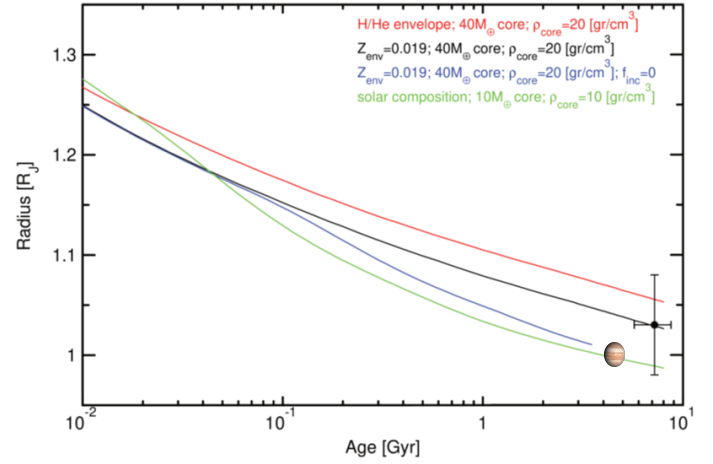


Fig. 15. Position of TOI-2529 *b* in the age-radius diagram (black dot). Planet evolutionary models with different envelope composition and insolation level over-plotted. For comparison, a simple model of Jupiter is also shown.

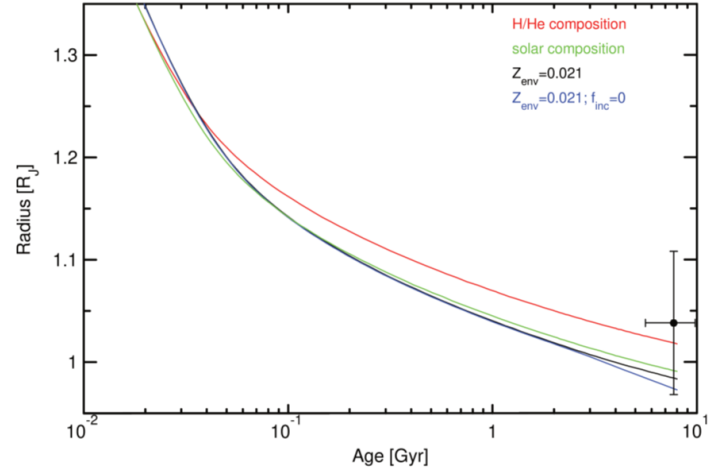


Fig. 16. Same as Fig. 15, but for TIC 4672985 *b*.

very well characterized transiting WJs. In terms of the orbital configuration, TOI-2529 *b* is found in a nearly circular orbit, which is consistent with an in situ formation channel via core-accretion (e.g., Bodenheimer et al. 2000; Boley et al. 2016; Batygin et al. 2016) or by a type II disk migration pathway (e.g. Lin & Papaloizou 1993). In this scenario, even in the case of a Jupiter-mass planet in a highly inclined and eccentric orbit (e.g., due to planet-planet interactions; Weidenschilling & Marzari 1996), the tidal interactions with the disk lead to a rapid damping (on timescales of about 10^3 yr) of the inclination and the eccentricity (Marzari & Nelson 2009). In addition, TOI-2529 *b* orbits a metal-rich star, following the well-known planet-metallicity correlation for gas giants orbiting FGK dwarf stars (Gonzalez 1997; Santos et al. 2004; Fischer & Valenti 2005; Adibekyan 2019; Osborn & Bayliss 2020), which is also valid for more massive evolved stars (e.g., Jones et al. 2016). This correlation provides strong observational support for the core-accretion formation model. Furthermore, based on our calculations, the planet composition is consistent with a rocky core and heavy

element enrichment with respect to its parent star, providing further evidence of a formation channel via core accretion. Given its low equilibrium temperature and relatively compact radius, TOI-2529 *b* has a very low transmission spectroscopy metric (TSM; [Kempton et al. 2018](#)) of ~ 5 , making this a very challenging system for a detailed atmospheric characterization study. On the other hand, we estimated a Rossiter-McLaughlin (R-M; [Rossiter 1924; McLaughlin 1924](#)) RV amplitude of $\sim 7 \text{ m s}^{-1}$ (assuming $i_{\star} = 90 \text{ deg}$; see eq. (1) in [Triaud 2018](#)), which is within the reach of stable instruments mounted on 8-meter-class telescopes (due to the relatively faintness of the target), such as ESPRESSO ([Pepe et al. 2021](#)). A low obliquity level would provide further observational support for the disk migration scenario (e.g. [Lin et al. 1996](#)), highlighting the importance of a future R-M characterization of this system.

For TIC 4672985 *b* we obtained the following orbital parameters: $P = 69.0480^{+0.0004}_{-0.0005} \text{ d}$, $M_p = 12.74^{+1.01}_{-1.01} M_J$, $R_p = 1.026^{+0.065}_{-0.067} R_J$, and $e = 0.018^{+0.004}_{-0.004}$. Additionally, we detected an RV trend at the $\sim 350 \text{ m s}^{-1} \text{ yr}^{-1}$ level, indicating the presence of either an outer BD companion in the system or a bound low-luminosity stellar companion. Thus, this is a unique system. It is the first warm transiting substellar companion that is located in the regime of super-Jupiters to brown dwarfs and has a precise mass and radius determination. Interestingly, TIC 4672985 *b* also presents a very low eccentricity, which is extremely rare among planets of its class. Moreover, this observational result challenges theoretical migration models, where unlike the case of lower-mass gas giants, a low eccentricity like this is not a direct indication of coplanar migration via disk interactions because even at low inclinations with respect to the disk, the eccentricity can be excited by this mechanism in this planetary mass regime ([Bitsch et al. 2013; Dunhill et al. 2013](#)). Similarly, the presence of an outer companion might induce eccentricity growth via Kozai-Lidov cycles ([Kozai 1962; Lidov 1962](#)) or through nearly coplanar apsidal precession resonances (e.g., [Anderson & Lai 2017](#)). Measuring the obliquity level for this object (predicted R-M amplitude of $\sim 8 \text{ m s}^{-1}$) is thus mandatory to further characterize the orbital configuration of the system. On the other hand, and due to its very low TSM of ~ 1 , it is not possible to perform a detailed atmospheric study of this planet. Finally, from our calculations, the position of TIC 4672985 *b* in the age-radius diagram is consistent with a coreless model with subsolar metallicity, meaning that no metal enhancement with respect to the parent star is present. This could be an indication that this object was formed by gravitational instability (e.g., [Boss 1997; Bate 2012](#)), as was shown to be the case for substellar objects more massive than $\sim 10 M_J$ ([Schlaufman 2018](#)).

Acknowledgements. The results reported herein benefited from collaborations and/or information exchange within NASA's Nexus for Exoplanet System Science (NExSS) research coordination network sponsored by NASA's Science Mission Directorate under Agreement No. 80NSSC21K0593 for the program "Alien Earths". We thank the Swiss National Science Foundation (SNSF) and the Geneva University for their continuous support to the planet search programs. This work has been in particular carried out in the frame of the National Centre for Competence in Research PlanetS supported by the SNSF under grants 51NF40_182901 and 51NF40_205606. This publication made use of The Data & Analysis Center for Exoplanets (DACE), which is a facility based at the University of Geneva dedicated to extrasolar planets data visualisation, exchange and analysis. DACE is a platform of NCCR PlanetS and is available at <https://dace.unige.ch>. This paper made use of data collected by the TESS mission and are publicly available from the Mikulski Archive for Space Telescopes (MAST) operated by the Space Telescope Science Institute (STScI). Funding for the TESS mission is provided by NASA's Science Mission Directorate. We acknowledge the use of public TESS data from pipelines at the TESS Science Office and at the TESS Science Processing Operations Center. Resources supporting this work were provided by the NASA High-End Computing (HEC) Program through the NASA Advanced Supercomputing (NAS) Division

at Ames Research Center for the production of the SPOC data products. This paper is based on data collected by the SPECULOOS-South Observatory at the ESO Paranal Observatory in Chile. The ULiege's contribution to SPECULOOS has received funding from the European Research Council under the European Union's Seventh Framework Programme (FP/2007-2013) (grant Agreement n° 336480/SPECULOOS), from the Balzan Prize and Francqui Foundations, from the Belgian Scientific Research Foundation (F.R.S.-FNRS; grant n° T.0109.20), from the University of Liege, and from the ARC grant for Concerted Research Actions financed by the Wallonia-Brussels Federation. The Cambridge contribution is supported by a grant from the Simons Foundation (PI Queloz, grant number 327127). The Birmingham contribution to SPECULOOS is in part funded by the European Union's Horizon 2020 research and innovation programme (grant's agreement n° 803193/BEBOP), from the MERAC foundation, and from the Science and Technology Facilities Council (STFC; grant n° ST/S00193X/1, and ST/W000385/1). This publication benefits from the support of the French Community of Belgium in the context of the FRIA Doctoral Grant awarded to MT. ML acknowledges support of the Swiss National Science Foundation under grant number PCEFP2_194576. MRS acknowledges support from the UK Science and Technology Facilities Council (ST/T000295/1) and support from the European Space Agency as an ESA Research Fellow. MTP acknowledges the support of the Fondecyt-ANID Post-doctoral fellowship No. 3210253. TT acknowledges support by the DFG Research Unit FOR 2544 "Blue Planets around Red Stars" project No. KU 3625/2-1. TT further acknowledges support by the BNSF program "VIHREN-2021" project No. KP-06-DV/5. DD acknowledges support from the NASA Exoplanet Research Program grant 18-2XRP18_2-0136, and from the TESS Guest Investigator Program grants 80NSSC22K0185 and 80NSSC23K0769. JC acknowledges support of the South Carolina Space Grant Consortium. RB acknowledges support from FONDECYT project 11200751 and from project IC120009 "Millennium Institute of Astrophysics (MAS)" of the Millennium Science Initiative. MU gratefully acknowledges funding from the Research Foundation Flanders (FWO) by means of a junior postdoctoral fellowship (grant agreement No. 1247624N).

References

- Adibekyan, V. 2019, *Geosciences*, 9, 105
 Albrecht, S. H., Dawson, R. I., & Winn, J. N. 2022, *PASP*, 134, 082001
 Anderson, K. R. & Lai, D. 2017, *MNRAS*, 472, 3692
 Baraffe, I., Chabrier, G., & Barman, T. 2010, *Reports on Progress in Physics*, 73, 016901
 Bate, M. R. 2012, *MNRAS*, 419, 3115
 Batygin, K., Bodenheimer, P. H., & Laughlin, G. P. 2016, *ApJ*, 829, 114
 Batygin, K. & Stevenson, D. J. 2010, *ApJ*, 714, L238
 Beaugé, C. & Nesvorný, D. 2012, *ApJ*, 751, 119
 Bitsch, B., Crida, A., Libert, A. S., & Lega, E. 2013, *A&A*, 555, A124
 Bodenheimer, P., Hubickyj, O., & Lissauer, J. J. 2000, *Icarus*, 143, 2
 Bodenheimer, P., Lin, D. N. C., & Mardling, R. A. 2001, *ApJ*, 548, 466
 Boley, A. C., Granados Contreras, A. P., & Gladman, B. 2016, *ApJ*, 817, L17
 Boss, A. P. 1997, *Science*, 276, 1836
 Brahm, R., Espinoza, N., Jordán, A., et al. 2019, *AJ*, 158, 45
 Brahm, R., Jordán, A., & Espinoza, N. 2017a, *PASP*, 129, 034002
 Brahm, R., Jordán, A., Hartman, J., & Bakos, G. 2017b, *MNRAS*, 467, 971
 Brahm, R., Nielsen, L. D., Wittenmyer, R. A., et al. 2020, *AJ*, 160, 235
 Brahm, R., Ulmer-Moll, S., Hobson, M. J., et al. 2023, *AJ*, 165, 227
 Bressan, A., Marigo, P., Girardi, L., et al. 2012, *MNRAS*, 427, 127
 Carmichael, T. W., Quinn, S. N., Zhou, G., et al. 2021, *AJ*, 161, 97
 Castelli, F. & Kurucz, R. L. 2003, in *Modelling of Stellar Atmospheres*, ed. N. Piskunov, W. W. Weiss, & D. F. Gray, Vol. 210, A20
 Chabrier, G. & Baraffe, I. 1997, *A&A*, 327, 1039
 Chabrier, G., Baraffe, I., Allard, F., & Hauschildt, P. 2000, *ApJ*, 542, L119
 Cutri, R. M., Skrutskie, M. F., van Dyk, S., et al. 2003, *VizieR Online Data Catalog*, II/246
 Delrez, L., Gillon, M., Queloz, D., et al. 2018, in *Society of Photo-Optical Instrumentation Engineers (SPIE) Conference Series*, Vol. 10700, Ground-based and Airborne Telescopes VII, ed. H. K. Marshall & J. Spyromilio, 1070011
 Demory, B.-O. & Seager, S. 2011, *ApJS*, 197, 12
 Dong, J., Huang, C. X., Dawson, R. I., et al. 2021, *ApJS*, 255, 6
 Dunhill, A. C., Alexander, R. D., & Armitage, P. J. 2013, *MNRAS*, 428, 3072
 Espinoza, N. & Jordán, A. 2016, *MNRAS*, 457, 3573
 Espinoza, N., Kossakowski, D., & Brahm, R. 2019, *MNRAS*, 490, 2262
 Ferguson, J. W., Alexander, D. R., Allard, F., et al. 2005, *ApJ*, 623, 585
 Fischer, D. A. & Valenti, J. 2005, *ApJ*, 622, 1102
 Foreman-Mackey, D., Agol, E., Ambikasaran, S., & Angus, R. 2017, *AJ*, 154, 220
 Fortney, J. J., Marley, M. S., & Barnes, J. W. 2007, *ApJ*, 659, 1661
 Freedman, R. S., Marley, M. S., & Lodders, K. 2008, *ApJS*, 174, 504
 Fulton, B. J., Petigura, E. A., Blunt, S., & Sinukoff, E. 2018, *PASP*, 130, 044504

- Gaia Collaboration. 2020, *VizieR Online Data Catalog*, I/350
- Gaia Collaboration, Brown, A. G. A., Vallenari, A., et al. 2018, *ArXiv e-prints* [arXiv:1804.09365]
- Gaia Collaboration, Vallenari, A., Brown, A. G. A., et al. 2022, *arXiv e-prints*, arXiv:2208.00211
- Ginzburg, S. & Sari, R. 2016, *ApJ*, 819, 116
- Gonzalez, G. 1997, *MNRAS*, 285, 403
- Grevesse, N. & Sauval, A. J. 1998, *Space Sci. Rev.*, 85, 161
- Grunblatt, S. K., Huber, D., Gaidos, E., et al. 2017, *AJ*, 154, 254
- Guillot, T. 2010, *A&A*, 520, A27
- Guillot, T., Burrows, A., Hubbard, W. B., Lunine, J. I., & Saumon, D. 1996, *ApJ*, 459, L35
- Hobson, M. J., Brahm, R., Jordán, A., et al. 2021, *AJ*, 161, 235
- Høg, E., Fabricius, C., Makarov, V. V., et al. 2000, *A&A*, 355, L27
- Howell, S. B., Everett, M. E., Sherry, W., Horch, E., & Ciardi, D. R. 2011, *AJ*, 142, 19
- Jackson, B., Greenberg, R., & Barnes, R. 2008, *ApJ*, 681, 1631
- Jenkins, J. M., Twicken, J. D., McCauliff, S., et al. 2016, in *Proc. SPIE*, Vol. 9913, *Software and Cyberinfrastructure for Astronomy IV*, 99133E
- Jones, M. I., Brahm, R., Espinoza, N., et al. 2019, *A&A*, 625, A16
- Jones, M. I., Jenkins, J. S., Brahm, R., et al. 2016, *A&A*, 590, A38
- Kaltenegger, L. & Sasselov, D. 2011, *ApJ*, 736, L25
- Kaufer, A., Stahl, O., Tubbesing, S., et al. 1999, *The Messenger*, 95, 8
- Kempton, E. M. R., Bean, J. L., Louie, D. R., et al. 2018, *PASP*, 130, 114401
- Kipping, D. M. 2013, *MNRAS*, 435, 2152
- Knierim, H., Shibata, S., & Helled, R. 2022, *A&A*, 665, L5
- Kochanek, C. S., Shappee, B. J., Stanek, K. Z., et al. 2017, *PASP*, 129, 104502
- Komacek, T. D., Thorngren, D. P., Lopez, E. D., & Ginzburg, S. 2020, *ApJ*, 893, 36
- Kozai, Y. 1962, *AJ*, 67, 591
- Kreidberg, L. 2015, *PASP*, 127, 1161
- Laughlin, G., Crismani, M., & Adams, F. C. 2011, *ApJ*, 729, L7
- Lidov, M. L. 1962, *Planet. Space Sci.*, 9, 719
- Lin, D. N. C., Bodenheimer, P., & Richardson, D. C. 1996, *Nature*, 380, 606
- Lin, D. N. C. & Papaloizou, J. C. B. 1993, in *Protostars and Planets III*, ed. E. H. Levy & J. I. Lunine, 749
- Mamajek, E. E. 2009, in *American Institute of Physics Conference Series*, Vol. 1158, *Exoplanets and Disks: Their Formation and Diversity*, ed. T. Usuda, M. Tamura, & M. Ishii, 3–10
- Marzari, F. & Nelson, A. F. 2009, *ApJ*, 705, 1575
- Mayor, M., Pepe, F., Queloz, D., et al. 2003, *The Messenger*, 114, 20
- McLaughlin, D. B. 1924, *ApJ*, 60, 22
- Mollière, P. & Mordasini, C. 2012, *A&A*, 547, A105
- Munari, U., Henden, A., Frigo, A., et al. 2014, *AJ*, 148, 81
- Osborn, A. & Bayliss, D. 2020, *MNRAS*, 491, 4481
- Paredes, L. A., Henry, T. J., Quinn, S. N., et al. 2021, *AJ*, 162, 176
- Paxton, B., Bildsten, L., Dotter, A., et al. 2011, *ApJS*, 192, 3
- Paxton, B., Cantiello, M., Arras, P., et al. 2013, *ApJS*, 208, 4
- Pepe, F., Cristiani, S., Rebolo, R., et al. 2021, *A&A*, 645, A96
- Petrovich, C. & Tremaine, S. 2016, *ApJ*, 829, 132
- Phillips, M. W., Tremblin, P., Baraffe, I., et al. 2020, *A&A*, 637, A38
- Pojmanski, G. 1997, *Acta Astron.*, 47, 467
- Queloz, D., Mayor, M., Naef, D., et al. 2000, in *From Extrasolar Planets to Cosmology: The VLT Opening Symposium*, ed. J. Bergeron & A. Renzini, 548
- Rasio, F. A. & Ford, E. B. 1996, *Science*, 274, 954
- Ricker, G. R., Winn, J. N., Vanderspek, R., et al. 2015, *Journal of Astronomical Telescopes, Instruments, and Systems*, 1, 014003
- Rogers, F. J. & Nayfonov, A. 2002, *ApJ*, 576, 1064
- Rossiter, R. A. 1924, *ApJ*, 60, 15
- Santos, N. C., Israelian, G., & Mayor, M. 2004, *A&A*, 415, 1153
- Sarkis, P., Mordasini, C., Henning, T., Marleau, G. D., & Mollière, P. 2021, *A&A*, 645, A79
- Saumon, D., Chabrier, G., & van Horn, H. M. 1995, *ApJS*, 99, 713
- Schlaufman, K. C. 2018, *ApJ*, 853, 37
- Scott, N. J., Howell, S. B., Horch, E. P., & Everett, M. E. 2018, *PASP*, 130, 054502
- Soto, M. G., Jones, M. I., & Jenkins, J. S. 2021, *A&A*, 647, A157
- Speagle, J. S. 2020, *MNRAS*, 493, 3132
- Spiegel, D. S., Burrows, A., & Milsom, J. A. 2011, *ApJ*, 727, 57
- Stassun, K. G., Oelkers, R. J., Paegert, M., et al. 2019, *AJ*, 158, 138
- Tayar, J., Claytor, Z. R., Huber, D., & van Saders, J. 2022, *ApJ*, 927, 31
- Thorngren, D. P. & Fortney, J. J. 2018, *AJ*, 155, 214
- Tokovinin, A. 2018, *PASP*, 130, 035002
- Tokovinin, A., Fischer, D. A., Bonati, M., et al. 2013, *PASP*, 125, 1336
- Toner, C. G. & Gray, D. F. 1988, *ApJ*, 334, 1008
- Triaud, A. H. M. J. 2018, in *Handbook of Exoplanets*, ed. H. J. Deeg & J. A. Belmonte, 2
- Ward, W. R. 1997, *Icarus*, 126, 261
- Weidenschilling, S. J. & Marzari, F. 1996, *Nature*, 384, 619
- Ziegler, C., Tokovinin, A., Briceño, C., et al. 2020, *AJ*, 159, 19
- 1 European Southern Observatory, Alonso de Córdova 3107, Vitacura, Casilla, 19001, Santiago, Chile
- 2 Instituto de Astronomía, Universidad Católica del Norte, Angamos 0610, 1270709, Antofagasta, Chile
- 3 Facultad de Ingeniería y Ciencias, Universidad Adolfo Ibáñez, Av. Diagonal las Torres 2640, Peñalolén, Santiago, Chile
- 4 Millennium Institute for Astrophysics, Chile
- 5 Data Observatory Foundation, Chile
- 6 Institute of Astronomy, KU Leuven, Celestijnenlaan 200D, B-3001 Leuven, Belgium
- 7 Department of Astronomy & Astrophysics, 525 Davey Laboratory, The Pennsylvania State University, University Park, PA, 16802, USA
- 8 Center for Exoplanets and Habitable Worlds, 525 Davey Laboratory, The Pennsylvania State University, University Park, PA, 16802, USA
- 9 Department of Physics, Engineering and Astronomy, Stephen F. Austin State University, 1936 North St, Nacogdoches, TX 75962, USA
- 10 Cerro Tololo Inter-American Observatory, Casilla 603, La Serena, Chile
- 11 Department of Physics and Astronomy, The University of North Carolina at Chapel Hill, Chapel Hill, NC 27599-3255, USA
- 12 Instituto de Astrofísica, Facultad de Física, Pontificia Universidad Católica de Chile, Santiago, Chile
- 13 Department of Physics & Astronomy, College of Charleston, 66 George Street Charleston, SC 29424, USA
- 14 School of Physics & Astronomy, University of Birmingham, Edgbaston, Birmingham B15 2TT, UK
- 15 Max-Planck-Institut für Astronomie, Königstuhl 17, 69117 Heidelberg, Germany
- 16 Department of Astronomy, Sofia University “St Kliment Ohridski”, 5 James Bourchier Blvd, BG-1164 Sofia, Bulgaria
- 17 Steward Observatory and Department of Astronomy, The University of Arizona, Tucson, AZ 85721, USA
- 18 Space Telescope Science Institute, 3700 San Martin Drive, Baltimore, MD 21218, USA
- 19 Wesleyan University, Middletown, CT 06459, USA
- 20 Department of Physics and Kavli Institute for Astrophysics and Space Research, Massachusetts Institute of Technology, Cambridge, MA 02139, USA
- 21 European Space Agency (ESA), European Space Astronomy Centre (ESAC), Camino Bajo del Castillo s/n, 28692 Villanueva de la Cañada, Madrid, Spain
- 22 Department of Astronomy, The Ohio State University, Columbus, OH, USA
- 23 Observatoire Astronomique de l’Université de Genève, Chemin Pegasi 51, 1290, Versoix, Switzerland
- 24 Physikalisches Institut, University of Bern, Gesellschaftsstrasse 6, 3012, Bern, Switzerland
- 25 Lowell Observatory, Flagstaff, AZ, USA
- 26 Department of Astronomy and Planetary Science, Northern Arizona University, Flagstaff, AZ, USA
- 27 Department of Physics and Astronomy, University of New Mexico, Albuquerque, NM, USA
- 28 Astrobiology Research Unit, University of Liège, Allée du 6 août 19, B-4000 Liège (Sart-Tilman), Belgium
- 29 AIM, CEA, CNRS, Université Paris-Saclay, Université de Paris, F-91191 Gif-sur-Yvette, France
- 30 Cavendish Laboratory, JJ Thomson Avenue, Cambridge CB3 0HE, UK
- 31 Department of Physics, ETH Zurich, Wolfgang-Pauli-Strasse 2, CH-8093 Zurich, Switzerland
- 32 NASA Ames Research Center, Moffett Field, CA 94035, USA
- 33 SETI Institute, Mountain View, CA 94043 USA
- 34 Center for Astrophysics | Harvard & Smithsonian, 60 Garden Street, Cambridge, MA 02138, USA
- 35 Department of Earth, Atmospheric and Planetary Sciences, Massachusetts Institute of Technology, Cambridge, MA 02139, USA

³⁶ Department of Aeronautics and Astronautics, Massachusetts Institute of Technology, 77 Massachusetts Avenue, Cambridge, MA 02139, USA

³⁷ Department of Astrophysical Sciences, Princeton University, Princeton, NJ 08544, USA

³⁸ El Sauce Observatory – Obstech, Chile

³⁹ NASA Exoplanet Science Institute, Caltech/IPAC, Mail Code 100-22, 1200 E. California Blvd., Pasadena, CA 91125, USA

Appendix A: Radial velocity tables.

Table A.1. Relative radial velocities for TIC 4672985.

BJD-2450000	RV (m s ⁻¹)	σ_{RV} (m s ⁻¹)	BVS (m s ⁻¹)	σ_{BVS} (m s ⁻¹)	Instrument
59222.54345	162.4	10.7	116.8	47.8	CHIRON
59225.59389	317.1	11.1	69.5	39.6	CHIRON
59229.60416	543.4	13.6	37.8	40.9	CHIRON
59234.56679	736.5	14.8	-2.3	44.5	CHIRON
59400.91392	-229.2	15.0	-65.8	54.0	CHIRON
59400.93624	-230.3	10.1	-1.0	38.5	CHIRON
59412.91660	-589.7	12.7	8.4	43.6	CHIRON
59417.83555	-567.8	13.0	-5.8	33.2	CHIRON
59422.89921	-364.9	10.9	16.6	39.8	CHIRON
59448.85994	619.4	9.7	-40.2	32.1	CHIRON
59452.81067	576.3	15.1	36.1	59.5	CHIRON
59459.83254	308.3	12.8	-156.0	61.5	CHIRON
59465.84358	-71.6	29.3	-79.6	122.5	CHIRON
59480.68472	-628.4	20.4	43.9	56.3	CHIRON
59489.73775	-467.5	25.4	65.5	73.7	CHIRON
59498.71994	-14.4	23.3	123.9	62.0	CHIRON
59501.70927	125.8	26.0	97.5	78.5	CHIRON
59504.66754	277.7	15.8	-59.1	39.9	CHIRON
59526.58391	354.7	9.3	50.0	37.3	CHIRON
59531.66372	70.9	12.1	17.0	28.2	CHIRON
59536.60366	-233.1	10.4	9.9	33.8	CHIRON
59593.53740	396.2	9.6	69.2	56.6	CHIRON
59846.76957	-264.5	10.5	3.6	41.2	CHIRON
59859.69126	264.4	12.4	-29.4	37.4	CHIRON
60179.88229	-1090.9	19.4	2.0	64.7	CHIRON
59188.55229	30419.6	7.2	-20.0	11.0	FEROS
59191.58077	30238.5	6.8	0.0	10.0	FEROS
59194.58783	30068.3	7.3	-8.0	11.0	FEROS
59196.54313	29967.6	6.1	-8.0	9.0	FEROS
59206.55663	29736.2	8.8	-15.0	12.0	FEROS
59212.57083	29818.2	7.5	-3.0	11.0	FEROS
59216.65293	29987.7	7.9	-6.0	11.0	FEROS
59218.57604	30070.2	6.6	-6.0	10.0	FEROS
59222.61173	30300.8	6.9	-4.0	10.0	FEROS
59223.63904	30323.7	8.0	-38.0	11.0	FEROS
59422.85717	29733.6	7.0	10.0	10.0	FEROS
59482.72687	29472.6	6.5	-6.0	10.0	FEROS
59484.79610	29479.8	6.4	0.0	10.0	FEROS
59486.77790	29536.5	6.5	-16.0	10.0	FEROS
59497.85912	30013.9	7.5	-12.0	11.0	FEROS
59502.77381	30248.3	7.1	-2.0	11.0	FEROS
59540.63774	29681.6	7.0	22.0	10.0	FEROS
59546.55133	29490.0	8.5	-28.0	12.0	FEROS
59553.59297	29417.6	7.3	-11.0	11.0	FEROS
59587.61015	30598.7	7.3	-21.0	11.0	FEROS
59171.68146	31052.9	12.2	-25.3	15.9	HARPS
59189.61998	30366.6	12.2	5.0	15.9	HARPS
59216.61051	30014.4	6.3	22.1	8.2	HARPS
59219.54050	30136.1	8.5	4.7	11.1	HARPS
59220.55062	30202.1	7.3	10.5	9.5	HARPS
59230.54004	30708.9	6.7	-18.4	8.8	HARPS
59245.52983	30917.9	10.1	-21.7	13.2	HARPS
59245.54129	30930.6	5.9	-23.6	7.6	HARPS
59250.53267	30747.0	4.5	-2.7	5.8	HARPS
59251.53713	30718.8	7.3	-11.2	9.5	HARPS
59254.52904	30533.4	5.5	-4.4	7.1	HARPS
59258.54084	30318.6	6.3	1.7	8.2	HARPS

Continue on the next page

Table A.1. Relative radial velocities for TIC 4672985.

BJD-2450000	RV (m s ⁻¹)	σ_{RV} (m s ⁻¹)	BVS (m s ⁻¹)	σ_{BVS} (m s ⁻¹)	Instrument
59470.82587	29821.6	7.8	34.2	10.2	HARPS
59490.73357	29642.7	9.2	-16.6	12.0	HARPS
59502.79276	30257.9	7.8	3.6	10.2	HARPS
59514.73359	30692.0	5.5	-1.8	7.1	HARPS
59531.60765	30218.5	7.8	-7.4	10.2	HARPS
59532.66751	30166.7	7.2	15.0	9.4	HARPS
59182.63980	30755.0	22.5	-77.1	31.9	CORALIE
59187.68617	30491.1	30.7	-57.1	43.4	CORALIE
59196.58888	29998.8	22.6	-6.7	31.9	CORALIE
59201.63030	29789.8	33.7	-56.6	47.7	CORALIE
59208.59669	29750.5	34.8	-61.9	49.2	CORALIE
59214.57535	29920.0	28.8	-42.3	40.7	CORALIE
59231.56773	30737.8	47.0	-22.3	66.4	CORALIE
59244.56099	30930.6	42.4	-39.8	59.9	CORALIE
59250.56540	30696.4	45.1	-15.0	63.8	CORALIE
59253.53569	30561.6	41.8	-39.7	59.1	CORALIE
59260.54649	30203.5	49.4	-63.1	69.9	CORALIE
59455.76669	30582.3	24.5	-25.7	34.7	CORALIE
59464.80650	30117.6	26.8	-37.1	37.9	CORALIE
59473.70146	29639.4	27.1	-72.8	38.3	CORALIE
59479.73983	29479.2	27.9	-32.4	39.5	CORALIE
59490.66775	29650.8	30.1	15.5	42.5	CORALIE
59504.69109	30325.1	25.2	-65.6	35.7	CORALIE
59512.75189	30639.3	23.7	-35.9	33.5	CORALIE
59521.56897	30607.6	44.0	-45.8	62.2	CORALIE
59542.62956	29577.4	29.2	-53.2	41.4	CORALIE
59580.60906	30522.8	22.7	-73.5	32.2	CORALIE
59609.57162	29634.5	20.4	-17.2	28.8	CORALIE
59825.83112	29165.8	22.7	-45.1	32.1	CORALIE
59826.78639	29191.5	17.0	-6.1	24.0	CORALIE
59846.81771	29855.9	50.8	14.0	71.8	CORALIE
59862.77739	30381.1	19.1	-70.7	27.0	CORALIE
59873.68405	30067.9	14.7	8.5	20.8	CORALIE
59893.66991	29137.4	18.6	-84.8	26.3	CORALIE
59918.58953	29950.6	12.6	-31.7	17.8	CORALIE

Table A.2. Relative radial velocities for TOI-2529.

BJD-2450000	RV (m s ⁻¹)	err (m s ⁻¹)	BVS (m s ⁻¹)	eBVS (m s ⁻¹)	instrument
59239.70586	46.5	10.3	33.1	44.2	CHIRON
59247.70453	-5.1	10.1	90.3	32.6	CHIRON
59249.60260	-24.7	12.8	41.4	35.8	CHIRON
59255.56122	-123.4	11.3	-0.8	32.3	CHIRON
59269.67164	-132.0	8.6	31.8	27.6	CHIRON
59279.55943	-79.3	12.4	-49.1	17.7	CHIRON
59291.66346	30.0	12.3	-37.1	28.5	CHIRON
59305.56255	6.8	15.2	-42.5	31.9	CHIRON
59345.50162	-18.4	13.3	16.8	38.8	CHIRON
59360.47119	17.0	12.7	-73.6	29.0	CHIRON
59474.86950	10.1	9.4	84.3	32.2	CHIRON
59483.88722	94.2	18.7	11.1	38.4	CHIRON
59491.85983	134.2	21.7	149.3	88.6	CHIRON
59498.87897	47.8	34.3	-29.0	74.9	CHIRON
59536.80881	-43.7	9.3	-12.1	22.9	CHIRON
59544.82069	-4.8	7.8	51.1	21.2	CHIRON
59551.73266	55.9	10.6	31.7	27.9	CHIRON
59559.83665	71.6	12.4	53.9	36.3	CHIRON
59566.73667	6.2	9.3	35.3	29.3	CHIRON
59597.72786	-65.5	13.2	-4.2	37.6	CHIRON
59603.60796	-24.0	7.6	14.0	20.8	CHIRON
59187.75268	21240.8	7.9	0.0	11.0	FEROS
59191.80547	21221.9	7.5	9.0	11.0	FEROS
59193.74595	21201.2	7.8	2.0	11.0	FEROS
59195.72076	21202.5	8.4	8.0	11.0	FEROS
59205.71383	21219.1	8.3	-6.0	11.0	FEROS
59209.73037	21221.3	8.9	9.0	12.0	FEROS
59216.75761	21286.7	8.6	-4.0	12.0	FEROS
59218.74168	21292.8	7.8	18.0	11.0	FEROS
59220.80439	21323.5	10.5	3.0	14.0	FEROS
59223.82981	21359.8	8.7	7.0	12.0	FEROS
59265.68708	21148.6	7.7	12.0	11.0	FEROS
59273.72703	21219.5	9.6	40.0	13.0	FEROS
59277.53902	21222.1	8.2	11.0	11.0	FEROS
59281.70796	21246.1	8.8	-28.0	12.0	FEROS
59283.71154	21280.7	8.2	5.0	11.0	FEROS
59577.78443	21227.7	9.4	1.0	12.0	FEROS
59578.78822	21206.3	7.8	11.0	11.0	FEROS
59227.25224	21389.9	3.8	22.0	5.0	HARPS
59231.23038	21406.4	3.6	18.0	5.0	HARPS
59234.21435	21402.2	3.8	12.0	5.0	HARPS
59238.21866	21382.9	5.6	10.0	7.0	HARPS
59244.20042	21344.0	3.8	36.0	5.0	HARPS
59247.19025	21321.2	4.9	14.0	6.0	HARPS
59254.20689	21206.1	3.6	26.0	5.0	HARPS
59256.16169	21224.0	4.0	15.0	5.0	HARPS
59260.15700	21189.4	4.3	6.0	6.0	HARPS
59263.19458	21175.3	5.2	19.0	7.0	HARPS
59268.17774	21194.2	6.4	16.0	8.0	HARPS
59280.11283	21273.6	5.2	37.0	7.0	HARPS
59291.16541	21372.6	4.9	16.0	6.0	HARPS
59295.17803	21403.2	11.2	39.0	15.0	HARPS
59364.98782	21413.3	5.2	6.0	7.0	HARPS
59369.00836	21371.7	7.4	4.0	10.0	HARPS
59371.00808	21369.3	8.6	26.0	11.0	HARPS
59372.94187	21374.3	8.0	3.0	10.0	HARPS
59505.36859	21341.4	5.9	1.0	8.0	HARPS
59506.36871	21300.0	5.2	22.0	7.0	HARPS
59518.32891	21206.2	4.8	16.0	6.0	HARPS
59533.28374	21230.7	4.9	21.0	6.0	HARPS
59562.26679	21365.7	10.3	-4.0	13.0	HARPS
59577.24623	21238.3	3.8	23.0	5.0	HARPS
59622.21689	21405.1	4.9	23.0	6.0	HARPS
59639.21249	21269.2	6.0	8.0	8.0	HARPS
59658.19716	21191.5	8.0	-2.0	10.0	HARPS

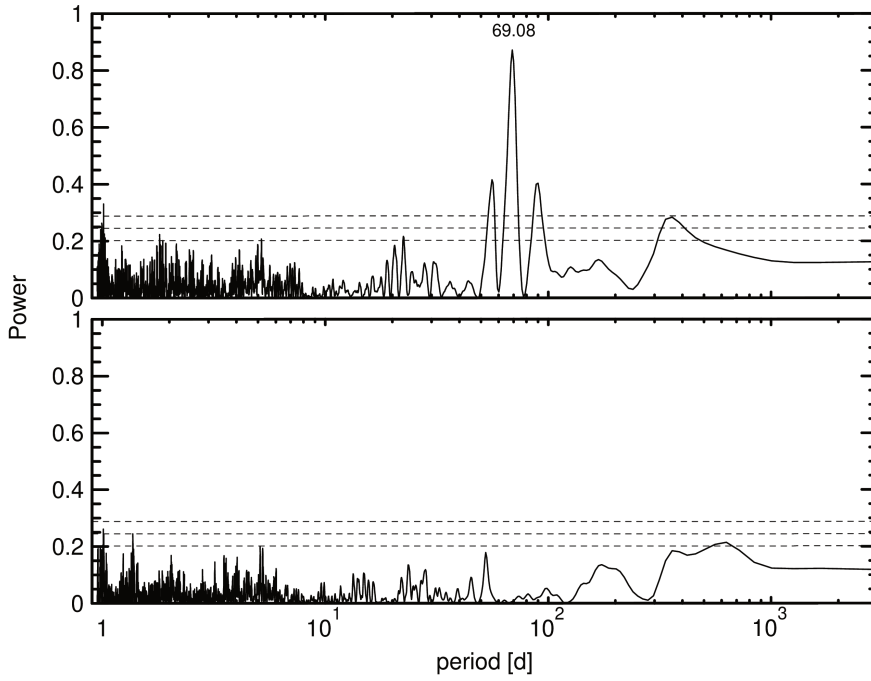


Fig. A.1. Upper panel: Periodogram of the combined RVs of TIC 4672985, after correcting by the long-term quadratic trend and applying the differential instrumental zero points. The dashed horizontal lines correspond to 10%, 1% and 0.1% false-alarm probability (from bottom to top). The period of maximum power is labeled. Lower panel: Periodogram of the post-fit residuals.

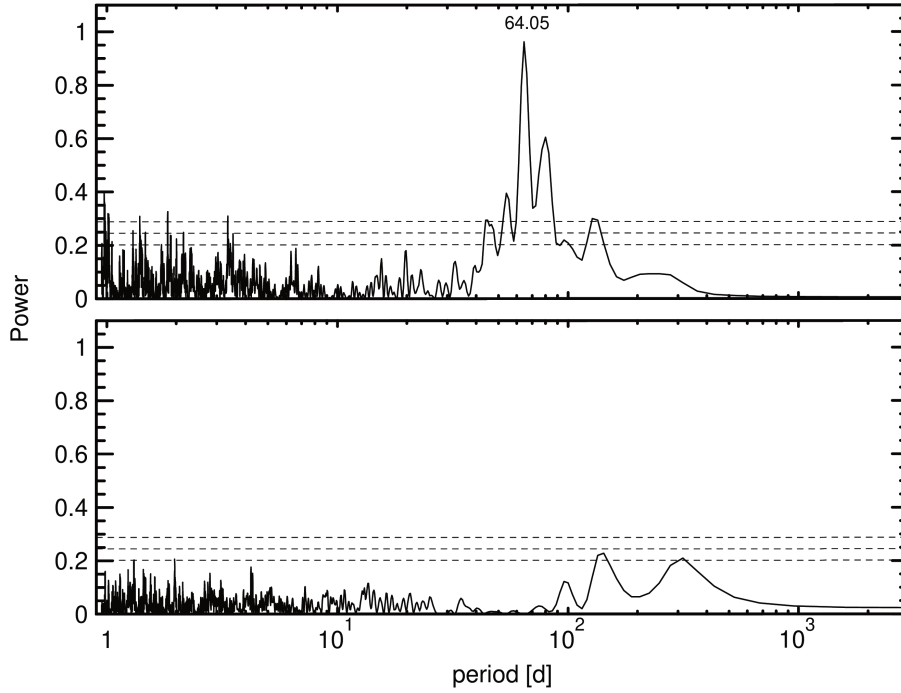


Fig. A.2. Same as for Fig. A.1, but for TOI-2529.

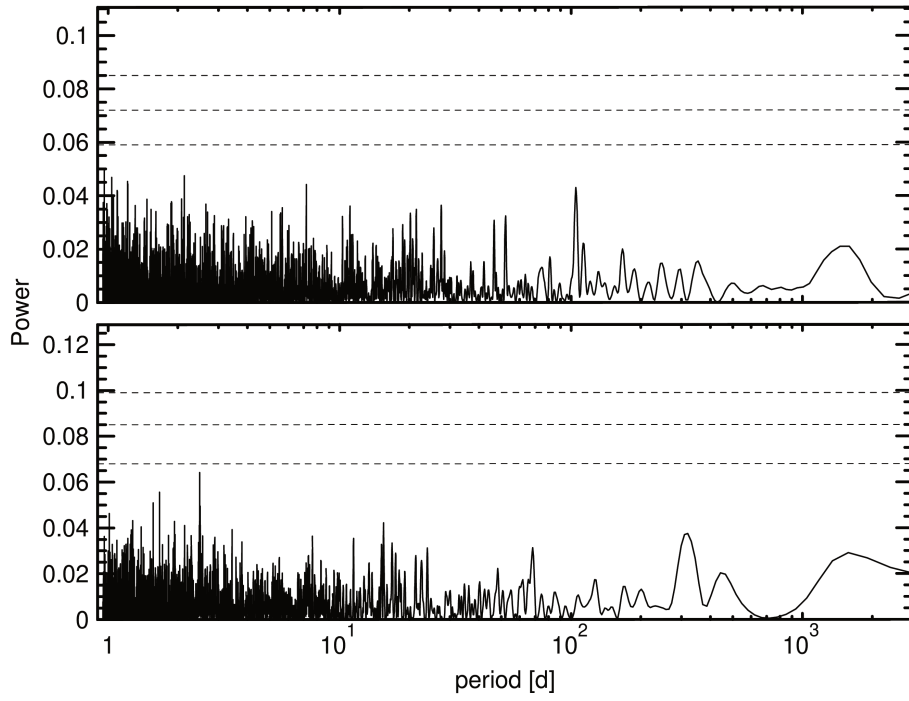


Fig. A.3. Periodogram of the ASAS and ASAS-SN V-band photometry of TIC 4672985 (upper and lower panel, respectively). The dashed horizontal lines correspond to 10%, 1% and 0.1% false-alarm probability (from bottom to top).

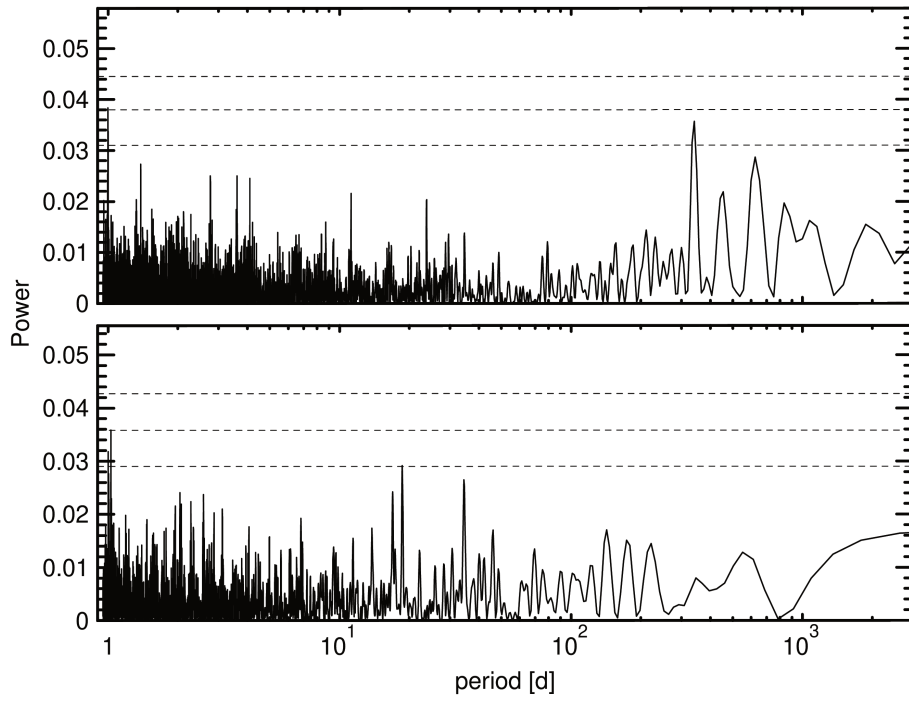


Fig. A.4. Same as for Fig. A.3, but for TOI-2529.